

AD-A135 891

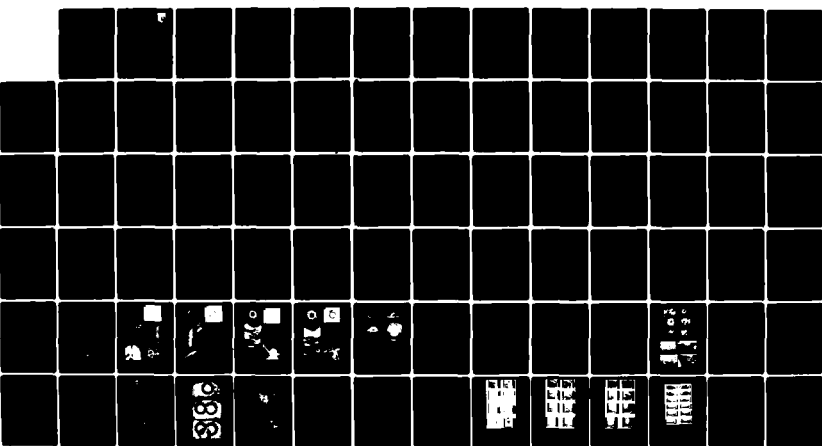
LIQUID IMPACT EROSION MECHANISMS IN TRANSPARENT
MATERIALS(U) CAMBRIDGE UNIV (ENGLAND) CAVENDISH LAB
J E FIELD ET AL. OCT 83 AFWAL-TR-83-4101 AFOSR-78-3705

1/1

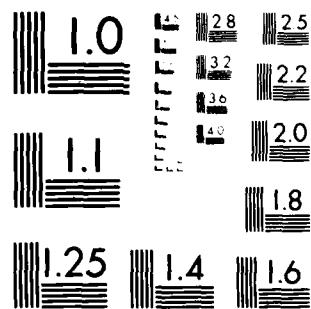
UNCLASSIFIED

F/G 17/5

NL



END
DATE FILMED
11-84
DTIC



MICROCOPY RESOLUTION TEST CHART
NATIONAL BUREAU OF STANDARDS 1963

AFWAL-TR-83-4101



LIQUID IMPACT EROSION MECHANISMS
IN TRANSPARENT MATERIALS

AUTHORS:

J. E. FIELD
S. van der Zwaag
D. Townsend
J. P. Dear

PHYSICS AND CHEMISTRY OF SOLIDS
CAVENDISH LABORATORY
MADINGLEY ROAD
CAMBRIDGE CB3 0HE UK

OCTOBER 1983

FINAL REPORT FOR PERIOD 30 SEPTEMBER 1980 TO 31 MARCH 1983

AD-A125-892

APPROVED FOR PUBLIC RELEASE; DISTRIBUTION UNLIMITED

MATERIALS LABORATORY
AIR FORCE WRIGHT AERONAUTICAL LABORATORIES
AIR FORCE SYSTEMS COMMAND
WRIGHT-PATTERSON AIR FORCE BASE, OHIO 45433

30013103
A

DTIC FILE COPY

83 12 16 074

NOTICE

When Government drawings, specifications, or other data are used for any purpose other than in connection with a definitely related Government procurement operation, the United States Government thereby incurs no responsibility nor any obligation whatsoever; and the fact that the government may have formulated, furnished, or in any way supplied the said drawings, specifications, or other data, is not to be regarded by implication or otherwise as in any manner licensing the holder or any other person or corporation, or conveying any rights or permission to manufacture use, or sell any patented invention that may in any way be related thereto.

This report has been reviewed by the Office of Public Affairs (ASD/PA) and is releasable to the National Technical Information Service (NTIS). At NTIS, it will be available to the general public, including foreign nations.

This technical report has been reviewed and is approved for publication.

G. F. Schmitt, Jr.

G. F. SCHMITT, JR
Project Engineer
Nonstructural Materials Branch

B. D. McConnell

B. D. McCONNELL, Chief
Nonstructural Materials Branch
Nonmetallic Materials Division

FOR THE COMMANDER

F. D. Cherry

F. D. CHERRY, Chief
Nonmetallic Materials Division

"If your address has changed, if you wish to be removed from our mailing list, or if the addressee is no longer employed by your organization please notify N-PAFB, OH 45433 to help us maintain a current mailing list".

Copies of this report should not be returned unless return is required by security considerations, contractual obligations, or notice on a specific document.

UNCLASSIFIED

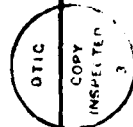
SECURITY CLASSIFICATION OF THIS PAGE (When Data Entered)

REPORT DOCUMENTATION PAGE		READ INSTRUCTIONS BEFORE COMPLETING FORM
1. REPORT NUMBER AFWAL-TR-83-4101	2. GOVT ACCESSION NO. A128891	3. RECIPIENT'S CATALOG NUMBER
4. TITLE (and Subtitle) Liquid Impact Erosion Mechanisms in Transparent Materials	5. TYPE OF REPORT & PERIOD COVERED Final Report 30 Sept. 1980-31st March 1983	
7. AUTHOR(s) J.E. Field, S. van der Zwaag, D. Townsend and J.P. Dear	6. PERFORMING ORG. REPORT NUMBER AFOSR-78-3705 D	
9. PERFORMING ORGANIZATION NAME AND ADDRESS Physics and Chemistry of Solids Cavendish Laboratory Madingley Road, Cambridge, CB3 OHE, UK	10. PROGRAM ELEMENT, PROJECT, TASK AREA & WORK UNIT NUMBERS Proj. 2422, Task 242201 WUN. 24220123, 62102F	
11. CONTROLLING OFFICE NAME AND ADDRESS Materials Laboratory (AFWAL/MLBT) AF Wright Aeronautical Laboratories, AFSC Wright-Patterson AFB, OH 45433	12. REPORT DATE October 1983	
14. MONITORING AGENCY NAME & ADDRESS (if different from Controlling Office) Materials Laboratory (AFWAL/MLBE) Wright-Patterson AFB OH 45433	13. NUMBER OF PAGES 82	
16. DISTRIBUTION STATEMENT (of this Report) Approved for public release; distribution unlimited.	15. SECURITY CLASS. (of this report) UNCLASSIFIED	
17. DISTRIBUTION STATEMENT (of the abstract entered in Block 20, if different from Report)		
18. SUPPLEMENTARY NOTES		
19. KEY WORDS (Continue on reverse side if necessary and identify by block number) Liquid Impact Erosion Fracture Zinc Sulphide Glasses Sapphire Germanium Hard Coatings		
20. ABSTRACT (Continue on reverse side if necessary and identify by block number) This project has been concerned with developing techniques for the study of liquid impact, with studying the behaviour of various infra-red transparent solids with analytic work on hard coatings and with basic studies of liquid/solid impact. Damage has been assessed quantitatively by measuring the 'residual' strength after impact and plotting strength against velocity of substrates with a hard coating. The protection offered by the coating is examined in terms of the elastic properties of the coating and its thickness. Section 2 reviews our recent liquid impact damage studies. Section 3 describes a study of the effect.		

UNCLASSIFIED

SECURITY CLASSIFICATION OF THIS PAGE(When Data Entered)

of thin coatings on the damage to brittle materials due to static and dynamic loading. Section 4 describes our basic work on liquid/solid impact in which techniques were developed for producing impacts of a solid with two-dimensional liquid shapes. This geometry allowed processes occurring inside the liquid to be followed in detail using high-speed photography. This section also contains an analytic model for the early stage of jet formation. ↙



A1

UNCLASSIFIED

SECURITY CLASSIFICATION OF THIS PAGE(When Data Entered)

	TABLE OF CONTENTS	PAGE
1.	INTRODUCTION	1
2.	LIQUID IMPACT DAMAGE ASSESSMENT FOR A RANGE OF INFRA-RED MATERIALS	3
	2.1 INTRODUCTION	3
	2.2 THE JET TECHNIQUE	4
	2.3 IMPACT DAMAGE IN BRITTLE MATERIALS ...	5
	2.4 RESIDUAL STRENGTH TESTING	6
	2.5 THEORY BEHIND THE RESIDUAL STRENGTH CURVE	9
	2.6 THRESHOLD VELOCITY FOR DIFFERENT JET AND DROP SIZES	11
	2.7 ON THE GRAIN DEPENDENCE OF THE FRACTURE TOUGHNESS OF ZINC SULPHIDE	12
	2.8 ON THE GRAIN SIZE DEPENDENCE OF MICRO-PLASTICITY IN ZINC SULPHIDE	14
	2.9 HARD COATINGS	16
	2.10 DISCUSSION	17
	(a) THE JET TECHNIQUE	17
	(b) RESIDUAL STRENGTH TESTING	18
	(c) ZINC SULPHIDE	18
	(d) HARD COATINGS	19
3.	INDENTATION AND LIQUID IMPACT STUDIES ON COATED GERMANIUM	20
	3.1 INTRODUCTION	20
	3.2 EXPERIMENTAL	21
	3.3 RESULTS	21
	(a) BALL INDENTATIONS ON COATED GERMANIUM ...	21
	(b) LIQUID JET IMPACT DAMAGE	22
	3.4 DISCUSSION	23
	(a) BALL INDENTATIONS ON COATED GERMANIUM ...	23
	(b) LIQUID JET IMPACT EXPERIMENTS ON COATED GERMANIUM	25
	3.5 CONCLUSIONS	25

	PAGE
4. AN INVESTIGATION OF THE SHOCK STRUCTURES AND THE CONDITIONS FOR JETTING DURING LIQUID IMPACT	27
4.1 INTRODUCTION	27
4.2 EXPERIMENTAL	29
4.3 RESULTS	31
(a) WEDGE IMPACT	31
(b) COMPLIANT TARGETS	33
4.4 JET VELOCITY	34
(a) THEORETICAL	34
(b) EXPERIMENTAL	37
4.5 CONCLUSION	38
APPENDIX	39
REFERENCES	40

LIST OF ILLUSTRATIONS

FIGURE		PAGE
1.	Relation between jet radius, R_j , and drop radius, R . The shaded area shows schematically the compressed liquid which generates the high pressures.	44
2.	Equivalent drop size as a function of impact velocity for jets of different sizes.	44
3.	Schematic diagram of the jet gun apparatus.	45
4.	Examples of impact damage in soda-lime glass due to jet impacts from a 0.4 mm nozzle. Equivalent to impacts with \sim 2 mm diameter drops. (a) 300 m s^{-1} , (b) 450 m s^{-1} , (c) 700 m s^{-1} .	45
5.	Micrographs obtained with a 0.8 mm jet impact at 175 m s^{-1} . (a) optical transmission micrograph of the impact damage. (The flaw leading to failure in the pressure tester is arrowed). (b) Micrograph with oblique reflective illumination; magnification as in (a). (c) and (d) enlargements of the areas marked in (a) and (b) respectively; magnification for (d) as in (c). (e) and (f) the specimen after failure in the pressure tester.	46
6.	Micrographs obtained with a 0.8 mm jet impact at 200 m s^{-1} . (a) Optical transmission micrograph of the impact damage. (The flaw leading to failure in the pressure tester is arrowed). (b) Micrograph with oblique reflective illumination; magnification for (d) as in (c). (e) and (f) the specimen after failure in the pressure tester.	47
7.	Micrographs obtained with a 0.8 mm jet impact at 300 m s^{-1} . (a) Optical transmission micrograph of the impact damage. (The flaw leading to failure in the pressure tester is arrowed). (b) Micrograph with oblique reflective illumination; magnification as in (a). (c) and (d) enlargements of the areas marked in (a) and (b) respectively; magnification for (d) as in (c). (e) and (f) the specimen after failure in the pressure tester.	48

8.	Micrographs obtained with a 0.8 mm jet impact at 500 m s^{-1} . (a) Optical transmission micrograph of the impact damage. (The flaw leading to failure in the pressure tester is arrowed). (b) Micrograph with oblique reflective illumination; magnification as in (a). (c) and (d) enlargements of the areas marked in (a) and (b) respectively; magnification for (d) as in (c). (e) and (f) the specimen after failure in the pressure tester.	49
9.	Cross-section of the 0.8 mm jet impact damage in zinc sulphide. (a) 175 m s^{-1} , (b) 300 m s^{-1} , (c) 400 m s^{-1} , (d) 600 m s^{-1} .	50
10.	Variation of the residual fracture stress with jet impact velocity for soda-lime glass. Jet from 0.8 mm orifice. Error bars indicate standard deviation of the mean.	50
11.	Same data as in Fig. 10 but now results for "undamaged" and damaged specimens plotted separately.	51
12.	Variation of failure probability with jet impact velocity. Same data as in Fig. 10. Estimated uncertainty $\pm 10\%$.	51
13.	Variation of residual fracture stress after single impact and multiple jet impact.	51
14.	Residual strength curve for ZnS for single impact with jets from a 0.8 mm nozzle.	52
15.	Equivalent flaw sizes for ZnS as a function of impact velocity.	52
16.	Residual strength curves for ZnS, a hot-pressed silicon nitride and single crystal sapphire impacted on the basal plane.	53
17.	Theoretical residual strength curve (—) and failure probability curve (---) for soda-lime glass, (see text).	54

18.	Theoretical residual strength curves for soda-lime glass (see text). o "as received specimens. ● "abraded" specimens.	54
19.	K_{Ic} versus (grain size) $^{-\frac{1}{2}}$ for ZnS.	54
20.	Surface views of Vickers indents on ZnS. All for loads of 100 N. (1) 2.5 μm grain size, (b) 6.5 μm , (c) 8 μm , (d) 32 μm (e) 140 μm and (f) 400 μm . See text for details.	55
21.	Grain dependence of the subsurface deformation mode for Vickers indentations on ZnS. (a) 300 N indentation for 0.5 μm grain size, (b) 75 N for 2 μm , (c) 150 N for 16 μm and (d) 100 N for 140 μm .	55
22.	Vickers hardness versus (grain size) $^{-\frac{1}{2}}$ for ZnS. Indenter load 10 N.	56
23.	Vickers hardness versus (grain size) $^{-\frac{1}{2}}$ for ZnS. Indenter load 100 N.	56
24.	Variation of the maximum radial stress at the interface with the coating parameters. P^* is the maximum axial stress in the coating surface, d is the coating thickness and a the radius of the contact zone.	57
25.	Variation of the maximum tensile stress at the coating surface with coating parameters. E_c and E_s are the Young's modulus of the coat and substrate respectively, v , is Poisson ratio. See reference 45 for further details.	57
26.	Velocity dependence of the diameter of the central zone for 2 mm drop (46) and jet (equivalent drop size ~4 mm) impact. The ratio is close to the factor 2 which would be predicted.	58
27.	Maximum crack depth for 2 mm drop (46) and jet (equivalent drop size ~4 mm) impact. The ratio is close to the factor 2 which would be predicted.	58

28. Variation of the load to form ring cracks as a function of ball radius for both uncoated and coated germanium. 59
29. Impact damage on uncoated germanium due to a 0.8 mm jet. Impact velocity 260 m s^{-1} . (a) damage after first impact, (b) damage after second impact, (c) damage after third impact. The letter A marks a common feature in each figure to aid in the comparison. 60
30. Impact damage on 3 μm coated germanium due to a 0.8 mm jet. Impact velocity 260 m s^{-1} as for Figure 29. 61
31. Damage due to three consecutive impacts at 220 m s^{-1} on (a) uncoated germanium, (b) 3 μm coated germanium. 62
32. Variation of pressure at which ring crack formed as a function of contact radius for both uncoated and coated germanium (same data as in Figure 28). 63
33. Ratio of the fracture pressure for coated and uncoated specimens as function of the normalised coating thickness (see text). 63
34. Impact of a drop with a target. The shock envelope is constructed from many individual wavelets. With a drop the angle β constantly changes. 64
35. Top and side views, not to scale, of the impact geometries. W is the liquid/gelatine wedge, P is the plastic sabot and S the impacting striker. In the initial experiments S was stationary and P was fired from a circular bore gun. In the final arrangement S was projected from a two-dimensional gun and higher impact velocities with W were achieved. 64
36. Impact geometries for a target striking a liquid wedge for (a) supersonic contact with the shock envelope attached to the contact point (b) subsonic contact with the primary shock advancing ahead of the contact point and a jet forming. 65

37. Impact with a wedge with β ca. 3° and $M_i = 0.1$. There is a supersonic contact point and no jetting in the wedge. A jet labelled J, forms only when the shock reaches the left-hand boundary. The jet velocity is ca. 200 m s^{-1} . Careful inspection of frame 5 shows an associated air shock. The dark region labelled T is due to cavitation. 66
38. Impact with a wedge ca. 6° and $M_i = 0.1$. This is very close to the critical value for β . A strong shock is formed. Again there is no jetting in the wedge but only when the shock reaches the left-hand boundary. The jet labelled J, has a velocity of ca. 2500 m s^{-1} . 67
39. Impact with the wedge with β ca. 12° , $M_i = 0.1$. The contact point is subsonic and the wave much weaker. 68
40. Impact with a compliant wedge with $\beta = 7.5^\circ$ and $M_i = 0.12$. Note there is a supersonic contact point and no jetting in the wedge. β_c for a rigid target at $M_i = 0.12$ is 6.8° . 69
41. Impact with a double-angled wedge with $\beta_o < \beta_c$ and variable in the range β_c to 90° . 65
42. Situation when the target surface has passed point A and jetting has commenced. The positions of the shock envelope and the corner waves from O and A are shown. 70
43. Region I from Figure 42 is redrawn together with its image region I'. The pressures on the various boundaries are indicated. 70
44. The x-component of the flow velocity plotted non-dimensionally in terms of position along the line AB (Figure 42) for various double-edge configurations. $R = 0$ corresponds to point A, and $R = 1$ to point B. Note the dramatic increase in V_x as $\beta_c (5.71^\circ)$ is approached
45. An example of impact with a double-edged wedge with β_o just sub-critical and $\beta = 45^\circ$. The arrows mark the jet which has a velocity of $600 \pm 100 \text{ m s}^{-1}$ in agreement with theory. 72

SECTION 1

INTRODUCTION

The research on this project has been concerned with developing techniques for the study of liquid impact, assessing the behavior of various infrared transparent solids, analytic and experimental work on hard coatings, and basic studies of liquid/solid impact.

As discussed in detail in our previous interim reports (1,2,3) we use three different techniques for studies of high velocity liquid/solid impact. The first involves projecting specimens of up to 25.4 mm diameter at stationary drops. The second fires a liquid jet at a stationary target. The third uses two-dimensional configurations (discs, wedges of liquid) which are impacted. The first approach is nearest to the practical situation in liquid impact; the second has distinct advantages in its ease of operation, low construction cost and the velocity range which can be covered. The final approach, using the two-dimensional configuration, allows processes occurring inside the impacted liquid to be followed by high-speed photography, and is nearer situations which can be theoretically analyzed.

In order to assess impact damage quantitatively, we measure "residual strengths". This involves impacting a specimen under known conditions and then measuring the strength. The advantages of this approach are that you have data on (i) the unimpacted specimen strength (ii) the threshold velocity for damage and (iii) the strength reduction following impact. A hydraulic apparatus, which stresses 2" (ca. 51 mm) diameter disc specimens, was initially developed for this work. The technique has subsequently been modified and improved. An apparatus for stressing discs of 1" (25.4 mm) diameter is proving useful where the amount of specimen material is limited or expensive.

Our earlier research has shown that it is possible to relate drop and jet impact in a useful manner, and to use the concept of an equivalent drop size for jet impacts. Our high-speed camera work (1) showed that our apparatus produces jets which are coherent and with smooth, curved front faces. Further since the high pressures of liquid impact occur in the first instant of impact, jet and drop impact can be made 'equivalent' to a reasonable approximation. The convenience of the jet impact technique compared with other approaches cannot be overemphasized. Our

jet apparatus is fully calibrated so that a particular jet size and velocity can be chosen and the collision achieved within a few minutes.

Section 2 reviews our recent liquid impact damage studies. The research has been concerned with a range of infra-red transmitting materials including zinc sulphide, germanium and saponine. Post impact 'residual strength' curves are presented, together with analytic work explaining the main features exhibited by the curves. The research on zinc sulphide has included a study of the effect of grain size on the hardness and K_{IC} values of the material.

Section 3 describes a study of the effect of thin hard coatings on the damage in brittle materials due to static and dynamic loading. The system studied was hard carbon layers on germanium. For quasi-static ball indentations, a significant increase in the load for ring crack formation was observed. The increase depends strongly on the ratio of coating thickness to ball radius. The results are in good agreement with theoretical predictions. Examination of the impact damage due to high velocity liquid jet impact showed only a small increase in rain erosion resistance.

Section 4 describes our recent basic work on liquid/solid impact. Techniques have been developed for producing impact of a solid with two-dimensional wedges of liquid. One attraction of the wedge geometry is that it maintains a constant angle between the liquid and the solid interfaces: this simplifies both the theoretical analysis and the experimental interpretation while retaining the essential features of the impact. Liquid wedge and drop geometries are produced by first casting a water/gelatine sheet and then cutting out the required shape. The impacting solid is a plate fired from a rectangular bore gas gun. The liquid is viewed at high magnification using high speed-photography at microsecond framing rates. The shocks in the liquid are made visible by use of Schlieren photography. Section 4 gives details of the new experimental techniques. The results give information on the shock structures produced, the 'water hammer' and 'edge' pressures and the critical conditions for jetting. A model for the early states of jet formation is presented. The impact geometries discussed relate to a range of practical situations including not only liquid impact erosion, but also explosive welding and the production of shaped-charge jets.

SECTION 2
LIQUID IMPACT DAMAGE ASSESSMENT FOR A RANGE OF INFRA-RED MATERIALS

2.1 INTRODUCTION

In this section we review the progress of our research on damage studies. Earlier work on this contract was described in (1-3). A useful review of our studies up to 1979 can be found in our paper at the 1979 Erosion Conference (4).

Forward-facing aircraft components may suffer damage due to the impact with rain drops. This damage may take the form of paint stripping, pitting of aerofoils, and failure of rivets (5). However, rain erosion is a more serious problem for brittle components, such as glass or plastic domes and covers and fiber reinforced plastic or ceramic radomes, where multiple drop impacts may result in catastrophic failure. In the case of brittle materials, the impact damage is primarily due to the interaction of the Rayleigh surface wave, which is generated during the impact, with pre-existing surface defects such as flaws and scratches (6). Such an interaction may lead to crack growth and subsequent material removal and strength reduction.

In the drop impact process two regimes can be distinguished. Firstly, an initial stage during which very high pressures are generated due to the compressible behavior of the liquid (7). These pressures for a rigid target are given by the equation $P = \rho CV$ where ρ is the liquid density, C , the shock wave velocity in the liquid, and V the impact velocity. They are the so-called "water hammer" pressures. It continues as long as the contact area between the impacting drop and the solid expands supersonically with respect to the waves in the liquid (see Section 4 of this report and 6, 8-11). The duration of this stage depends on the impact velocity and the radius of curvature of the drop but is generally in the range of 0.1 - 1 μ s. In the second stage of the impact, the shock waves generated by the impact move up the free surface of the drop, jetting begins, and the impact pressure drops to lower values due to incompressible flow. Incompressible flow pressures P_i are of the order $\frac{1}{4} \rho V^2$. For a 500 $m s^{-1}$ impact, the incompressible flow pressure is only about 10% of the

pressure generated in the compressible phase. Most of the impact damage in brittle materials is associated with the initial high-pressure regime. It is for this reason that liquid jets with a smoothly curved front profile can be used to simulate drop impact to a reasonable accuracy.

A considerable amount of research has been performed at Cambridge (see, for example 1-3, 12, 13) to place the jet technique on a quantitative basis and to be able to relate jet to drop impact. For reasons discussed in detail in the earlier references, the radius of the region over which a drop produces water-hammer pressure is less than the drop radius and is given by $r \leq \frac{RV}{C}$ where R is the drop radius and V and C are as defined earlier. On the other hand, a jet (essentially a coherent cylinder of liquid) produces the high pressures over the full cylinder head radius. Thus for normal impact (i.e. at right angles to the target surface) a smaller radius jet simulates a larger radius drop. Figure 1 illustrates this point. Curves giving the "equivalent drop" size for different sized jets plotted as a function of impact velocity are reproduced in figure 2.

2.2 THE JET TECHNIQUE

The jet technique, in which jets are fired at a stationary specimen, has great operational advantages over the more realistic but very complicated experiment of projecting a specimen at a stationary drop. The high velocity water jets used in the present experiments were produced by a technique originally developed in the laboratory by Bowden and Brunton (14) and subsequently modified and improved (3, 12, 13). In this technique, a lead slug is fired with an 0.22" calibre air-rifle into the rear of a water-filled stainless steel chamber. The forward motion of the sealing neoprene disc extrudes the water at high velocity through the orifice section at the front of the chamber. Figure 3 illustrates the jet production apparatus. The most important part of the design is the nozzle section of the chamber from which the jet emerges. The jet velocity is approximately 5 times the projectile velocity, but the most important requirement is to produce coherent jets with a smooth, slightly curved front profile. The whole system is calibrated, using high-speed photography, so that it is only necessary to choose a suitably dimensioned chamber and set a firing pressure for a jet of chosen velocity to be produced. High-speed photographs of jets were illustrated in references (3, 12).

2.3 IMPACT DAMAGE IN BRITTLE MATERIALS

The impact damage in brittle materials consists of a central undamaged zone surrounded by an annular region with circumferential cracks. The dimensions of the damaged area as well as the extent of the cracking depend on the impact velocity. This is illustrated in figure 4 which shows jet impact damage on soda-lime glass for three impact velocities. For the highest impact velocity the central zone appears to be damaged due to subsurface cracking at the rear surface. The cracks are due to the propagation of defects in the surface because of their interaction with the tensile stress component of the Rayleigh wave generated by the impact. The central undamaged zone is due to the fact that at the initial stages of the impact the contact area, in which all stresses are compressive, expands at a higher velocity than the Rayleigh wave velocity.

This central undamaged zone and the ring of circumferential cracks are shown more clearly in figures 5-8 which illustrate jet impact damage on chemically deposited zinc sulphide. It can be seen that within the annular region, the average crack size tends to increase with radial distance from the center of the impact while at the same time the density of the cracks decreases. This variation is due to the changes in the amplitude and duration of the Rayleigh wave with radial distance: initially the wave amplitude is very high but its duration is extremely short ($< 0.1 \mu s$). Under these conditions a very small flaw size is sufficient to cause crack growth but the amount of growth is small because of the short duration of the pulse. When the Rayleigh wave expands outwards its amplitude decreases but its duration increases. A larger initial defect size is now required for propagation but when this happens a considerable amount of growth occurs. Therefore, the largest and most serious flaw will almost always be found at the outer edge of the damaged zone. At very large distances the stress pulse amplitude has decreased so much that none of the defects surrounding the impact site will grow.

Examination of the damage patterns has shown that in this material there are two types of defects: a high density of very small defects which are responsible for the large number of small cracks, and much rarer large defects which lead to very large final crack sizes, such as the ones shown in figure 5. While the second type of defects are due to grinding, polishing, and handling damage, the

first type of defects seem to be related to the grain size. For the fine grained material shown here, the average initial size will be small but their density high. Finally we would like to draw attention to the damage caused by a jet impact at 600 m s^{-1} (figure 9d). In this specimen the amplitude of the reflected bulk wave was sufficiently high to cause cracking at the rear surface. This form of damage, which is called spalling, is only important for unsupported thin specimens.

2.4 RESIDUAL STRENGTH TESTING

Although optical examination of drop/jet impact damage is very important, only qualitative information can be obtained. Field et al (3, 12) have therefore used the post-impact strength of brittle specimens as a quantitative measure of the impact damage. They have developed a bursting technique, in which the specimen is hydraulically loaded to failure (15, 16). This technique, in which a circular symmetric stress field of almost constant strength is generated over a large part of the specimen surface, ensures that all the flaws extended by the impact are sampled at equal stress. Only very low stresses are felt by the edges of the specimen so that "edge" failures are almost entirely eliminated.

The results of the combined jet and post-impact strength testing technique are shown in figure 10 for soda-lime glass. The specimens (50 mm diameter, 3 mm thick) were subjected to a single normal jet impact. The impact velocity has been varied between 125 and 700 m s^{-1} .

The residual strength curve obtained shows that a critical velocity has to be reached before a reduction in the average fracture stress is observed.

This threshold velocity is followed by a transition region ($150 - 300 \text{ m s}^{-1}$) in which the average fracture stress decreases rapidly with increasing impact velocity. At high impact velocities the average fracture stress is a much weaker function of the impact velocity. It should be pointed out that for impact velocities between 150 and 300 m s^{-1} a large scatter in the results is obtained. Some specimens have a very low fracture stress while others fail at a fracture stress comparable to unimpacted specimens. The percentage of specimens with a low fracture stress increases with impact velocity. At impact velocities above 400 m s^{-1} , all specimens

fail at a low fracture stress. To show this aspect more clearly the average fracture stresses for the two groups are plotted separately in figure 11. The data can also be expressed in terms of the probability that the fracture strength of the specimens is reduced by the impact. The probability curve for single impact is shown in figure 12. It should be stressed that the variability of the results in the transition region is not caused by lack of reproducibility in the impact but is due to the inherent variation of the surface flaw distribution between individual specimens. As pointed out by Matthewson and Field (16) the fracture stress can also be used to calculate the effective size of the flaw causing failure of the specimen. In general, the equivalent flaw size, c , can be calculated from the fracture stress, σ_f , and the critical stress intensity factor, K_{Ic} , using

$$c = \alpha(K_{Ic}/\sigma_f)^{1/2} \quad 2.1$$

where α is a dimensionless constant depending on the flaw and the stress field geometry. In the present work, the crack geometry is taken as semi-circular for this type of crack in a uniaxial bending stress field $\alpha = 0.75$. Inserting in the above equation the appropriate values for the stress intensity factor ($K_{Ic} = 0.75 \text{ MN m}^{-3/2}$) and fracture stress ($\sigma_f = 100 \text{ MPa}$), an average flaw size of about 42 μm for unimpacted specimens is found. This value agrees quite well with the inherent flaw dimensions of 34 μm reported by Mecholski et al (17). The slightly larger value obtained here probably arises from slow crack growth during testing of the specimens in the pressure tester (test duration typically 30 s). For the impacted specimens we calculate flaw dimensions of 100 to 1500 μm for specimens impacted at 300 or 700 m s^{-1} respectively, which is in good agreement with observations.

We have also examined the residual strength curve of soda-lime glass as a function of the number of impacts. The results (figure 13) show that for damaged specimens the average fracture stress as well as the width of the transition region decreases with the number of impacts. The threshold velocity for impact damage was unchanged by the number of impacts. Although the increase in damage with the number of impacts seems hardly surprising, it should be mentioned that there is a large difference between static and dynamic loading. In quasi-static loading with a rigid sphere, the dimensions of the resulting cone crack are entirely determined by the material

properties and the applied load. A re-application of the same load, assuming no stress corrosion or frictional effects, does not extend the crack beyond its initial size. However, in the dynamic case the extent of the crack growth is not only determined by the magnitude of the stress pulse but also by its duration, which is in the case of drop or jet impact often the limiting factor. Subsequent impacts effectively give further time for crack growth and the jet continues to develop until K_{IC} is no longer exceeded at the crack tip.

So far it has been assumed that the damage is only due to the interaction of the Rayleigh wave with pre-existing surface defects. However, longitudinal waves reflected from the rear surface can enhance the Rayleigh wave and increase the crack growth. The position at which this occurs depends on the relative wave velocities and the specimen thickness (6). It has been found that this process makes a significant contribution to the impact damage of thin soda-lime specimens at high impact velocities. By supporting the specimens with an acoustically coupled thick glass block an increase of about 15 MPa in the fracture stress of specimens impacted at 600 m s^{-1} was obtained (13). No statistically significant effects were found at low impact velocities. It should be emphasized that soda-lime glass has a low attenuation coefficient for stress waves and that many materials will not be susceptible to these reinforcement effects until correspondingly higher impact velocities.

Using this technique we have also examined other materials such as silicon nitride (4), zinc sulphide; Raytheon material (figures 14, 15) sapphire and germanium. Figure 16 compares the residual strength curves for hot-pressed silicon nitride (HPSN), sapphire and zinc sulphide. A full discussion of the behavior of ZnS can be found in reference (18). Clearly the sapphire has the highest initial strength, though the threshold velocity for the material tested is below that of HPSN. Both the sapphire and HPSN retain some strength up to high velocities. The dramatic fall in the sapphire curve is not surprising since it has a low toughness and a very high fracture velocity. The maximum fracture velocity is two or three times greater than that of ZnS and HPSN. Thus once a defect starts to extend it grows much further in sapphire during the time of the loading pulse.

2.5 THEORY BEHIND THE RESIDUAL STRENGTH CURVE

Of paramount importance for the damage is the magnitude and time dependence of the Rayleigh surface wave. Measurements by Swain and Hagan (19) have shown that the Rayleigh wave can be approximated, to a reasonable accuracy, by a triangular pulse. The absolute magnitude of the pulse could not be determined but these workers have suggested that the amplitude will be approximately proportional to the impact velocity, by drawing an analogy with quasi-static contact problems where the stress field scales linearly with the applied pressure. Secondly, one needs to know the equation for the stress intensity factor of a non-stationary crack. Of the various functions derived we have chosen the equation for the stress intensity factor derived by Eshelby (20) which is particularly applicable to the problem of propagating small flaws and which is given by

$$K_{ld} = m \sigma (\pi a)^{\frac{1}{2}} (1 - V/C_R)^{\frac{1}{2}} U \quad 2.2$$

where m is a geometrical constant, a the initial flaw size, V the current crack velocity, C_R the Rayleigh wave velocity and U is given by the following series

$$U = 1 + \frac{3}{8} \frac{c-a}{a} - \frac{15}{256} \left(\frac{c-a}{a} \right)^2 + \dots \quad 2.3$$

where c is the current crack size. Evaluation of this series shows that for $c < 20a$, U can be accurately approximated (21) to

$$U = \left[1 + \frac{4}{5} \frac{c-a}{a} \right]^{\frac{1}{2}} \quad 2.4$$

The current crack velocity in the above equation can be derived from the experimentally determined dependence of the crack velocity on the dynamical stress-intensity factor (22).

$$V = V_{\max} (1 - K_{lc}^2 / K_d^2)^{\frac{1}{2}} \quad 2.5$$

where V_{\max} is the maximum crack velocity.

Finally, one needs to consider the probability density function for the flaw dimensions. We have used a simplified function derived by Jaytilaka and Trustrum (23) which is given by

$$f(c) = \frac{c_0^{n-1}}{(n-2)!} c^{-n} e^{-c_0/c} \quad 2.6$$

where c_0 is the size of the most probable flaw dimension. The parameter n is related to the Weibull parameter.

By combining the above functions one can calculate, to a first order approximation, the residual strength curve of brittle materials. The procedure we used has been described in detail elsewhere (13). It calculates the amount of crack growth for each of the flaws present in a "specimen" and compares the pre- and post-impact fracture strength. The procedure has been performed for a large number of specimens and impact velocities.

The results of the calculations have been plotted in the form of a residual strength curve in figure 17. A very good qualitative agreement with the residual strength curve for single impact is obtained. In particular the variation in the amount of scatter in the fracture stress as a function of the impact velocity is well-reproduced in the analysis. From the analysis a failure probability curve can be obtained which is also shown in figure 17 (broken line). Once again a good qualitative agreement with the measured probability curve is obtained. The model has also been used to calculate the effect of multiple impacts on the resulting damage and the same conclusions as from the experimental results can be made, namely an almost constant threshold velocity, a reduction of the width of the transition region and a continuous increase in the post-impact flaw size at high impact velocities.

The model can also be used to illustrate the effect of abrasion on the residual strength curve. For this purpose a new set of specimens with twice the density of flaws was generated. Furthermore, the size of the most frequent defect was increased. The impact parameters and material properties were the same as used for figure 17. The residual strength curves for the "as received" (open circles) and the "abraded" specimens (closed circles) are plotted in figure 18. Due to the abrasion not only the initial strength of the specimens is reduced but also the threshold velocity and the post impact strength at high impact velocities. The failure probability curve (not shown) shows a much smaller transition region for the "abraded" specimens. The above predictions are in very good agreement with experimental data for jet impact studies. Furthermore, Wiederhorn and Lawn (24) noted similar effects for solid particle impacts on abraded and unabraded glass specimens.

2.6 THRESHOLD VELOCITY FOR DIFFERENT JET AND DROP SIZES

The interaction between a stress pulse and a flaw is complex, depending on whether the pulse length is greater than, equal to or less than the flaw. Based on measured threshold strength values for glasses for a variety of jet sizes (0.4 to 1.6 mm) we have found that the criteria $\sigma^2 \tau = \text{constant}$ works well for the range studied (12) where σ is the applied stress and τ its duration. σ is simply linked to the "water hammer pressure" ΔV and τ , for a cylindrical jet, $= d/2C$. Thus for two different sized jets we obtain

$$\frac{V_2}{V_1} = \sqrt{\frac{d_1}{d_2}} \quad 2.7$$

However, if relatively high impact velocities are involved a more sophisticated expression is required. This is because the shock velocity C is a function of pressure. For the velocity range of interest $C = C_0(1 + 2V/C_0)$ where C_0 is the acoustic velocity (25). The equation now becomes

$$\frac{V_2(C_0 + 2V_2)^{\frac{1}{2}}}{V_1(C_0 + 2V_1)^{\frac{1}{2}}} = \sqrt{\frac{d_1}{d_2}} \quad 2.8$$

However, this correction only becomes greater than a few % for impact velocities greater than a few hundred metres per second.

In the case of drops, the pressures are again of the order ΔV but the diameter of the contact circle, D , over which these high pressures apply depends on both the drop diameter and the impact velocity (6) i.e. $D = dV/C$.

The duration of this high pressure regime is given by

$$\tau \sim \frac{3}{4} \frac{dV}{C^2} \quad 2.9$$

For two different sized drops, we have after use of the $\sigma^2 \tau = \text{constant}$ relation

$$\frac{V_2}{V_1} = \left(\frac{d_1}{d_2} \right)^{1/3} \quad 2.10$$

Note this expression is valid for both the acoustic approximation and when allowance is made for the shock correction.

Essentially this is because, for a drop, $\sigma^2 \tau$ does not depend on C (it cancels). For a cylindrical jet, $\sigma^2 \tau$ does depend on C .

Much of our residual strength data has been obtained with jets from an 0.8 mm orifice. This can be converted to an equivalent drop size using earlier results. We can then calculate threshold

damage values for any required drop size by using equation 10. Table 1 summarises threshold data for a range of materials.

Table 1 Threshold velocities / m s⁻¹

Materials	Threshold for 0.8 mm jet	Equivalent drop size / mm	Estimated for 1 mm drops
ZnS (Raytheon)	125	5	170
Soda-lime glass	150	5	205
Germanium	150	5	205
Sapphire (Basal plane)	350	4.4	455
Hot-pressed Silicon Nitride	00	4	630

2.7 ON THE GRAIN SIZE DEPENDENCE OF THE FRACTURE TOUGHNESS OF ZINC SULPHIDE

The dependences of the yield, flow and fracture stresses on grain size have been examined for a large number of ceramics. However, the number of studies on the effect of the grain size on the fracture toughness K_{Ic} is relatively small (26-32). The results obtained are often contradictory. In particular in the case of alumina some experiments have shown an increase in K_{Ic} with increasing grain size (26, 28) while in other experiments no grain size dependence (32) or even a decrease with increasing grain size (33) has been found. It has been shown by Simpson (34) and Pratt (30) that the grain size dependence obtained depends also on the type of test. In the present work we have determined the fracture toughness of polycrystalline zinc sulphide using the Vickers indentation technique developed by Lawn and Fuller (35). In this technique the length of the crack, C , formed by a load P is related to K_{Ic} by the equation

$$K_{Ic} = \frac{xP}{372}$$

where $x = (\tau^{3/2} \tan \psi')^{-1}$, $\psi' = \psi + \tan^{-1} \mu$, μ is the coefficient of friction and ψ the indenter semi-angle (68°). While the fracture toughness determined in this way may not be equal to the intrinsic fracture toughness (30) this test should give a good indication of the toughness of the material during solid particle erosion involving elastic-plastic contact. The specimens were produced by a chemical vapour deposition process. The average diameter

of the columnar grains ranged from 2 to 500 μm . For each specimen the scatter in the grain size was small.

The results obtained are plotted in figure 19. The figure shows that in the range of 500 to 8 μm grain size K_{Ic} increases approximately linearly with the reciprocal root of the grain size. For grains smaller than about 8 μm K_{Ic} decreases again.

The observed linear relationship between K_{Ic} and $d^{-\frac{1}{2}}$ agrees with a model for the grain size dependence of K_{Ic} assuming a non-thermally activated grain boundary deformation process (36). Also from the "crack nucleation through dislocation pile-up" model it can be argued that K_{Ic} will be approximately proportional to $d^{-\frac{1}{2}}$, as has been pointed out by Kawatake and Izumi (37). Earlier experiments in the laboratory on the relationship between microplasticity and Vickers indentation induced cracks in zinc sulphide (38) have confirmed that plastic deformation processes play a very important role in the initiation and propagation of these cracks. The decrease in K_{Ic} for very small grain sizes is attributed to the fact that grain boundary deformation is such that voids are formed in a spherical zone under the contact area (38). Further, towards the crack tip the deformation is less severe but might still lead to a microscopic loss of coherence at the grain boundaries, resulting in a decrease in the fracture toughness.

Micrographs of the indents made on different grain size material are shown in figure 20. All of the indents correspond to a load of 100 N. There is a clear change in the pattern of fracture as the grain size varies. For the smallest grain size of 2.5 μm , (illustrated in figure 20a) the "classic" pattern for this loading geometry is observed. Essentially the same pattern is followed for the 6.5 and 8 μm grain size material. However, for the grain sizes greater than 8 μm , there are no recognisable "median cracks", but instead multiple radial fractures. For these specimens, the diameter of the fracture zone was taken for the value of $2c$ in the expression for K_{Ic} .

Referring again to figure 19 we see that the points to the left of the maximum correspond to the formation of an irregular zone of radial fracture and those to the right to the symmetrical median crack growth. It could be argued that the K_{Ic} values given for the large grain material are suspect since the crack system does

not correspond to the one analysed. This is a valid point. However, in our view the lower "effective" K_{Ic} values with larger grain sizes still illustrate an important trend, since they are a measure of the extent of fracture produced by a given load. More is said about this when the hardness data has been described (see below).

3.4 ON THE GRAIN SIZE DEPENDENCE OF MICRO-PLASTICITY IN ZINC SULPHIDE

Hardness has long been recognised as an important property of ceramics, in particular in applications involving friction, wear and abrasion. The microplastic deformation processes also play an important role in the nucleation of the various crack systems associated with elastic-plastic contact in these nominally brittle materials (32, 38, 39-42). In this study, cross-sectional examination of the deformation processes underneath Vickers indentations was made by producing indentations across the interface of two polished specimens held rigidly together in cold mounting plastic (38). After indentation the specimens were prised apart and the subsurface deformation was studied optically. The axis of the columnar grains was perpendicular to the cross-sectional plane. Hardness measurements were made with a Vickers micro-hardness tester. Various indenter loads were used.

The changes in the subsurface deformation with varying grain size are shown in figure 21. Figure 21a shows the deformation for a 300 N indentation on 0.5 μm diameter zinc sulphide. Within the deformed zone a large number of well-defined spiral flow lines can be distinguished which follow the maximum shear stress trajectories as predicted for an isotropic plastic material (43). Figure 21b illustrates the deformation in zinc sulphide with a grain size of 2 μm . Although the flow lines are still discernible, they are less well-defined than in the previous figure. Detailed examination of the subsurface deformation in these fine-grained specimens (38) has shown that intergranular voids are formed along the flow lines due to a grain boundary sliding process. Although deformation within the grains themselves takes place, a large part of the deformation is concentrated in the spiral flow lines. For the coarser grain sizes, the possibility of deformation along the grain boundaries is limited and the deformation occurs mainly within the grains.

In this case no spiral flow lines will be formed as is shown in figure 21c and d. In particular in figure 21d (grain size 1-4 μm) it is clear that the deformation is concentrated within the grains. The amount of slip in each grain depends on the orientation of the crystal with respect to the indentation stress field. For the 10 μm grain size (figure 21e) the deformation is more uniform in a large number of primary intergranular cracks.

These changes in mode of deformation also affect the various crack systems which form around the indentation. For the fine grained material well-defined median cracks form. These can be seen in the cross-section views (figure 21a and b) and in the surface views (figure 20). For the larger grain sizes (8 μm), the intergranular radial cracks showed a large scatter in length and fracture path. Furthermore, it was observed that at low loads the formation of lateral cracks in large grained materials was suppressed. It is proposed that due to extensive cracking in the deformed zone in these materials the compressed central zone can relax relatively easily upon unloading, leaving insufficient stored energy to propagate lateral cracks into the surrounding matrix. It should be pointed out that the absence of lateral cracking could reduce the rate of material removal during solid particle erosion. This is a point we would like to investigate in future research.

Hardness data for the different grain sized specimens is presented in figures 22 and 23. Figure 22 is for an indenter load of 10 N and figure 23 for an indenter load of 100 N. The minimum in the first case is at 20 μm and in the second at 160 μm . This factor 3 difference is very reasonable. It appears that the minimum occurs when the size of the indent is typically a few grain diameters.

For the 10 kg load the indent area is 10 x bigger and so its diameter is $\sqrt{10}$ (i.e. ~ 3) times larger. The increasing hardness towards smaller grain sizes is also reasonable since grain boundaries cause dislocation pile-ups. This is the Petch mechanism which predicts $H = H_0 + a d^{-\frac{1}{2}}$ where a is constant and d is the grain diameter. Figures 22 and 23 were plotted in terms of $d^{-\frac{1}{2}}$ to test this relation.

In figure 23 we show two dotted curves to the left of the minimum (i.e. towards larger grain sizes), the experimental spread in this area is such that both could be argued to be significant. Note that in a d^{-1} plot this region is rather compact although it covers a very wide range of grain size. The much larger scatter is not surprising since the indent size is now less than the grain size so that orientation effects will contribute to the spread of data.

2.9 HARD COATINGS

Until recently nearly all coating materials used to improve the rain erosion resistance of brittle aircraft components were either metallic or elastomeric. However, there are now several practical applications (e.g. infrared transparent windows) where traditional coating materials cannot be used because of unsuitable electromagnetic properties. The range of materials with the required optical properties is restricted to certain semiconductors, ceramics and amorphous materials. Generally, these substances are brittle materials with a relatively high Young's modulus.

In order to determine the feasibility of protecting brittle substrates against drop impact with a thin coating of a (brittle) material with a high Young's modulus, we have developed a static finite element model in which an undeformable sphere is loaded onto a coated halfspace. This simple approach to the very complex drop impact problem can be justified by the observed similarities between quasi-static ball indentation damage and liquid drop impact damage.

In the analysis we have concentrated on the stresses responsible for the failure of brittle materials namely the radial tensile stresses.

The model has been described in detail elsewhere (44) and we will just summarize the most important results here. It has been found that thin coatings of a rigid material can reduce the maximum radial tensile stress generated in the substrate from which it can be concluded that hard coatings can indeed be used to protect brittle materials against elastic contact damage. The reduction of the maximum tensile stress in the substrate (which occurs at the interface) is plotted in figure 24 as a function of the normalized coating thickness for various coating materials. The figure shows that a high Young's modulus of the coating material is particularly important in obtaining a large reduction in the tensile stresses and that a very thin coating can be sufficient.

The favourable effect of the coating on the substrate stresses is however accompanied by a strong increase in the maximum tensile stress which develops in the coating surface as is shown in figure 25.

This effect is due to the relatively large strains in the substrate which tend to "overstretch" the coating material.

The maximum stress increases rapidly with coating thickness for small coating thicknesses. At larger coating thicknesses the maximum tensile stress reaches a maximum and then decreases again.

In conclusion, the analysis has shown that materials with a high Young's modulus should be effective coating materials, provided their mechanical properties are good enough to withstand the high stresses in the coating itself. Although the range of Poisson's ratios for hard materials is rather small, materials with a relatively high Poisson's ratio (about 0.3) should be chosen since both the maximum substrate and the maximum coating stress decrease with increasing Poisson's ratio.

When considering the optimum coating thickness it should be noted that the analysis indicates two regions of preferable coating thicknesses, namely very thin ($d/a < 0.05$) or relatively thick coatings ($d/a < 0.4$). However, for these thick coatings the problem of spontaneous coating debonding due to residual stresses is a serious one.

For the thin coatings, a sizeable reduction in the substrate stresses can be obtained without too large an increase in the coating stresses. Ball indentation experiments on carbon coated germanium have shown that a coating thickness of 1 or 3 μm can increase the critical load for ring crack formation by as much as 100% and 200% respectively (for a detailed account see section 3 and reference 45).

2.10 DISCUSSION

(a) The Jet Technique

The pressures which cause liquid impact damage are those generated during the very initial stages of impact when compressible behaviour of the liquid occurs. For the impact velocities likely to arise in most rain erosion situations, the ratio of incompressible to compressible pressures is very small ($\sim 1/33$ at 100 m s^{-1} , $\sim 1/10$ at 500 m s^{-1}). This is the basic reason why jet simulation of drop

impact works reasonably well. It is essential though to produce jets which are coherent and which have a smooth, slightly curved, front profile.

Figures 26 and 27 compare jet and drop data for ZnS. The drop data is from Adler (46) the jet data from our own work (47). The drop data is for a 2 mm diameter drop. The jet data is for jets from a 0.8 mm nozzle which at 400 ms^{-1} (the middle of the range studied simulate a 4 mm drops). In other words the diameter of the central zone in the damage pattern (figure 26) and the maximum crack depth (figure 27) should be approximately 2 x greater for the jet compared with the drop as is indeed found.

We have also used the technique of projecting a specimen at a suspended drop. This has allowed us to test our drop/jet equivalence curves (figure 2). There is no doubt that the jet technique has enormous advantages in case of experimentation and low construction cost compared with methods using moving specimens. We are currently developing a multiple jet impact device which we feel could have great benefits for rain erosion testing.

We are presently studying the equivalence of jet and drop impact for angled impacts. It should be emphasised that the curves of figure 2 are for normal impact and need some modification for angled impacts.

(b) Residual Strength Testing

We believe that the quantitative data which these curves give is invaluable. An important new result is that multiple impact does not affect the threshold velocity (figure 13). Thus, a meaningful estimate of the threshold velocity under practical conditions can be obtained from single impact experiments.

(c) Zinc Sulphide

Grain size affects both the K_{Ic} (figure 20) and the hardness (figures 22, 23) of ZnS. Another important factor appears to be the hydrogen content of the specimen and we hope to report on that shortly. There is clearly great scope for future developments with this material to improve its erosion threshold.

The residual strength curve for the ZnS studied (Raytheon) material is shown in figure 14. The mean strength in our hydraulic test was $\sim 80 \text{ MPa}$ though some specimens had strengths greater than 100 MPa. As noted earlier specimen strength is often adversely affected by rather large flaws produced during surface preparation. If strengths of $\sim 100 \text{ MPa}$ were the mean rather than the exception this would significantly improve the threshold velocity for damage of this material.

(d) Hard Coatings

Theoretical and experimental studies have shown that relatively thin (few micron) layers of strong, high modulus coatings can significantly improve the threshold conditions for damage. This is clearly an area well worth further study.

SECTION 3

INDENTATION AND LIQUID IMPACT STUDIES ON COATED GERMANIUM

3.1 INTRODUCTION

Germanium is an important lens material for optical systems working in the infrared part of the spectrum since it combines good optical properties with a reasonable mechanical strength (48, 49). However, as in other brittle materials, the contact with either sharp or blunt particles can lead to crack formation and hence strength reduction. The type of damage depends on the applied load and the radius of curvature of the indenting particle (50). In the case of elastic-plastic contact, as occurs for sharp particles, several crack systems (radial, median and lateral cracks) can form at different stages of the loading cycle. In the literature there exists some controversy about the precise origin of these cracks. Evans et al (51-53) assume that the nuclei for these cracks are pre-existent while Hagan et al. (38, 41, 54, 55) have stressed the possibility of crack nucleation due to plastic deformation processes in nominally brittle materials. For germanium the relation between plastic deformation and associated cracking around sharp indents has been examined by Bannerjee and Feltham (56) and Lankford and Davidson (57).

In purely elastic contact, as occurs in large diameter ball indentation, a ring crack is formed around the contact area which upon further loading propagates into a cone crack (see Lawn and Wilshaw (58) for an extensive review). The inherent surface defects in brittle materials form the nuclei for these cracks. The driving force for the propagation of these defects is provided by radial tensile stresses which exist in a shallow surface layer outside the contact zone.

Recently, it has been shown theoretically (44) that the maximum radial stress generated in the substrate by a spherical indentation can be reduced with a thin rigid coating. Certain hard, anti-reflection coatings are of interest with germanium since they allow infrared transmission which soft, (for example, elastomeric), coatings would not. In particular, for coating materials with a very high Young's modulus a significant increase in the fracture load for the substrate is predicted. The reduction in maximum tensile stress

also depends strongly on the effective coating thickness, i.e. the ratio of coating thickness and contact radius. Therefore, in the present work we have examined the critical load for ring crack formation in carbon coated germanium as a function of coating thickness and radius of curvature of the indenting particle.

Furthermore, we have examined the beneficial effects of thin carbon coatings on the amount of damage due to high velocity rain drop impacts. This form of dynamically elastic loading can cause significant damage to brittle forward-facing aircraft components.

3.2 EXPERIMENTAL

The effect of thin hard coatings on the fracture load for ball indentations was examined for germanium specimens (25 mm diameter, 2 mm thick) provided with hard carbon coatings of 1 and 3 μm thickness. Tungsten carbide balls (0.4 and 1.0 mm diameter) and hardened steel balls (2.0 and 4.0 mm diameter) were used as indenters. The load was applied with an Instron testing machine. The cross-head speed during loading was 0.05 mm min^{-1} . The maximum load was applied for about 10 s. The occurrence of ring crack formation was determined by examining the surface with an optical microscope after unloading.

The liquid jet impact technique which was used to simulate high velocity ($> 100 \text{ m s}^{-1}$) rain drop impact has been described in section 2. The impact damage on both coated and uncoated specimens was assessed using optical microscopy.

3.3 RESULTS

3.3a Ball indentations on coated germanium

Examination of the contact damage at high loads on both coated and uncoated germanium showed an approximately hexagonally shaped "ring" crack. The ring cracks were usually visible on the coating surface. However, in a very limited number of cases at low loads only subsurface cracking could be detected, suggesting that for these coated specimens crack propagation started in the substrate. In the case of 0.4 mm ball indentations radial cracks as well as cone cracks were formed. Also plastic deformation and occasionally coating debonding was observed for this ball diameter. Therefore, these results fall outside the scope of the present work which is concerned with the effect of coatings for the case of purely elastic contact.

Detecting the onset of cracking in an optically transparent material is relatively easy since the contact area can be viewed directly. The procedure adopted here was to determine the load, at which 50% of the indents showed partial or complete ring cracks. This load is plotted in figure 28 as a function of the indenter radius for both uncoated and coated specimens. The results are based on about 30 indents per data point. In particular for the larger ball sizes complete shattering of the specimen occurred frequently making an accurate measurement of the fracture load impossible. The figure shows that a carbon coating can lead to a significant increase in the fracture load. For the 1 μm coating the increase is about 100% and for the 3 μm coating at least 200%.

3.3b Liquid Jet Impact Damage

Figure 29 shows the damage due to single and multiple liquid jet impact at 260 m s^{-1} for uncoated germanium. The damage is typical of that for brittle materials and consists of a central undamaged zone surrounded by an annular region with short circumferential cracks. The damage is due to the interaction of the Rayleigh surface wave generated by the impact and surface defects (5). The influence of the {111} cleavage plane orientation on the fracture pattern is well illustrated in this figure. The figure also shows the increase in impact damage with increasing number of impacts. For the first and second impact cleavage fracture is the most important mode of erosion. During the third impact the lateral outflow of water caused dislodgement of already existing raised cleavage edges and gross material removal. Such a sequence of erosion mechanisms has also been observed in multiple raindrop impact experiments on polycrystalline and single crystal germanium (59).

Figure 30 shows the impact damage for a 3 μm coated specimen also impacted at 260 m s^{-1} . The light area in this figure is the debonded region due to the outflow of water. For the first and second impact the number of cracks formed is smaller than for the uncoated specimen. At the third impact the increase in damage is considerable particularly in the debonded areas where there is a local loss of protection.

A more favourable influence of thin coatings on the get impact damage was observed at lower impact velocities. Figures 31a and 31b show the damage due to three successive impacts at 120 m s^{-1} for an uncoated and a $3 \mu\text{m}$ coated specimen respectively. For the uncoated specimen an almost complete ring of cracks was formed at each impact. However, for the coated specimen only a few isolated cracks could be detected in the coating. No subsurface cracking was observed (for these thin coatings subsurface cracking would have been easily detectable). At this lower impact velocity no signs of incipient coating.

At an impact velocity of 260 m s^{-1} the $1 \mu\text{m}$ thick coating gave less reduction in the damage than the $3 \mu\text{m}$ coating. However, no significant coating debonding occurred. For the lower impact velocity no significant differences between the damage for $1 \mu\text{m}$ and that for $3 \mu\text{m}$ coatings were observed.

3.4 DISCUSSION

3.4a Ball indentations on coated germanium

In this section we compare the measured increase in the fracture load of coated specimens with the results of our recent theoretical study on the effect of thin hard coatings on the Hertzian stress field (44). In order to enable the comparison with the theory we have replotted in figure 32 the data if figure 28 as the fracture pressure versus the contact radius. The contact radius was calculated using the well-known Hertzian equation

$$a^3 = \frac{4}{3} FR \left(\frac{1-v_1^2}{E_1} + \frac{1-v_2^2}{E_2} \right) \quad 3.1$$

where a is the contact radius, F the applied load, R the ball radius and v_1 , v_2 and E_1 , E_2 the Poisson's ratio and Young's modulus of the indenter and substrate respectively. We have taken $E = 140 \text{ GPa}$ and $v = 0.20$ as the average values for the elastic constants for germanium. It has been shown theoretically that for these thin coatings equation (1) gives a good approximation of the true contact radius on coated specimens. For the uncoated specimens the fracture pressure and hence the fracture stress, decreases continuously with increasing ball size and hence contact radius. This indenter size effect is due to an increased probability of stressing a flaw of sufficient size with larger sampled area.

The rapid decrease of the fracture pressure with contact radius for the coated specimens is due to a combination of two effects: (i)

the usual decrease of the fracture pressure with contact radius as observed for the uncoated specimens and (ii) the simultaneous decrease of the effective coating thickness (ratio of layer thickness, a , to the contact radius) which determines its protective influence. To separate the two effects and to obtain a good indication of the protection provided by the coating, we have plotted in ... the ratio of the fracture pressure for coated specimens, P , and that for an indentation with the same contact radius on an uncoated specimen, P^* , versus the normalised or effective coating thickness d/a . This procedure was followed to correct for the increase in contact area (and hence the decrease in fracture pressure because of flaw statistics reasons) at the increased loads for the coated specimens. The error bars in this figure are related to the uncertainties in the fracture loads indicated in figure 28. Figure 33 shows an approximately linear increase of the normalised fracture pressure with effective coating thickness. The increase in fracture pressure for the 0.4 mm ball indentations (where elastic-plastic contact takes place) is considerably smaller than predicted from the linear dependence observed for the larger ball sizes.

To compare the measured increase with theoretical predictions we have to estimate the elastic properties of the carbon film since no experimental values are yet available. It has often been found that the Young's modulus of disordered systems is about 80% of that of the crystalline state (60). Taking diamond as the reference state we expect a Young's modulus of about 800 GPa. On the other hand it has been found experimentally that the Young's modulus of thin amorphous films of germanium and silicon (which have the same structure as diamond) is only 30% of the crystalline value (61). For the present coating material this would give a Young's modulus of about 300 GPa. In figure 33 we have plotted (dashed lines) the theoretically predicted increase in the fracture pressure for three different coating moduli (300, 500 and 800 GPa) while assuming that the critical pressure is determined by substrate failure. The Poisson's ratio of the coating was taken as 0.20. Ignoring the two data points for 0.4 mm balls, where plastic deformation took place, a surprisingly good agreement between theory and experiment is obtained.

3.4b Liquid jet impact experiments on coated germanium

The threshold damage velocity for 0.8 mm jets is 150 m s^{-1} (62). Optical examination of the surface damage due to liquid jet impact has shown that there is some protection provided by the carbon coating. Due to the limited number of specimens available we were unable to determine quantitatively the increase in threshold velocity for impact damage as a function of coating thickness. However, the relatively small changes in damage patterns due to these coatings suggest that only a modest increase in the threshold velocity is obtained. Furthermore, the observations have shown a rapid loss of protection at higher impact velocities due to coating debonding caused by the shearing action of the radial outflow. This phenomenon, which has also been observed for drop impact experiments on coated zinc sulphide (63), will be a major problem for real rain erosion conditions where the number of impacts per unit area will be high. Finally, it was noted that the thin coating seemed almost as effective as the thick coating but less susceptible to debonding. Two points are likely to be significant here. The first is the practical problem of depositing thick coatings without residual stresses which make the coatings prone to debonding. The second is that liquid jet impact is a particular severe form of loading combining high normal and shear stresses. In particular, due to the outflow of water the shear stresses generated at the interface will be very much higher than under identical solid particle impact conditions.

3.5 CONCLUSIONS

It has been shown that the critical load for spherical indentations to form ring cracks in germanium can be significantly increased (up to 200% increase) by means of a thin carbon coating. The increase in the fracture load depends strongly on the effective coating thickness. The results are in good agreement with theoretical predictions. In the case of liquid jet impact the reduction in impact damage was more modest. Coating debonding due to lateral outflow was a major limitation of the coating system in particular for larger coating thicknesses. Although a coating may be of marginal advantage during liquid jet impact it can still assist in maintaining the pristine state of the surface so that the material performs better when impact does take place. The coating also has an important

role as an anti-reflection layer. The rather different behaviour of the coating in ball indentation and liquid jet impact experiments has shown that care should be taken in making quantitative predictions on coating performance under dynamic loading conditions from quasi-static experiments.

SECTION 4
AN INVESTIGATION OF THE SHOCK STRUCTURES
AND THE CONDITIONS FOR JETTING DURING LIQUID IMPACT

4.1 INTRODUCTION

As is well known, the collision between a liquid mass and a solid surface can generate high transient pressures and cause significant damage, particularly if the impact velocity is high. The high pressures have been attributed to compressible behaviour in the liquid. The fact that numerous situations exist in which such collisions occur has made the study of liquid impact crucial for the further development of related technologies. However, despite considerable activity in the subject there exists a large number of unexplained and poorly understood phenomena associated with liquid impact (11). The reasons for this are connected with the fact that the high pressures and much of the damage formation takes place during a very short time period following the initial contact, and as we will show, involve a complex dependence on the geometry of the liquid and solid surfaces in the contact area.

Considerable progress has been made in overcoming these obstacles by making extensive use of high speed photographic techniques and rapid response crystal guages. One result of this work is that when a curved liquid drop strikes a solid, the highest pressures do not occur at the center of impact where the normals to both the liquid and solid surfaces are parallel but on a nearly circular boundary at a distance which depends on the drop radius and the velocity of impact (11, 64, 65). Another result is that after an interval comparable to the time it takes the drop to spread out to the maximum pressure radius, a "jetting" motion develops. In certain impact speed ranges this jet has been observed to have a speed up to ten times the impact speed (66-69).

The study of these events has been considerably complicated by the fact that for the drop sizes normally used in experiments, which are typically up to a few millimetres in diameter, both the "jetting" and high pressure thresholds are reached when the intercept angle between drop edge and solid surface is, at most, a few degrees. Thus it becomes difficult to interpret the photographic evidence, and to observe the detailed behaviour of the liquid in the critical zone.

The main object of the present investigation was to overcome these experimental difficulties by the use of a technique designed to isolate the behaviour of the liquid in the critical zone and to prolong the duration of the critical period between the attainment of maximum "edge" pressure and "jetting". The rationale of our method is based on the mechanics of wave fronts spreading through the drop during the initial collision period (1, 11). The liquid is compressed by the collision, and the compression is signalled to the unaffected portions of the drop by waves moving at sonic speeds and even considerably exceeding the sound speed in the undisturbed liquid. One of these waves will be attached to the spreading edge contact point and, as first observed by Heymann (8), this will be a shock which can be calculated by the use of conservation laws. Such a calculation shows that the edge pressures can easily obtain values exceeding the normal impact pressure (8, 10, 70). Thus a crucial aspect of any liquid impact involves this attached shock. The present experiments are designed to study how the impact parameters of collision velocity and surface geometry influence this wave system. In particular we shall be concerned with how such a shock system can become detached from the solid surface, and how this detachment process leads to the formation of "jetting".

Lesser (10, 70) has carried out significant extensions of Heymann's work which shows that the shock system at the edge of a spreading spherical drop and the plane shock developed on a two-dimensional wedge-shaped impact surface are in a certain sense equivalent. This equivalence applies exactly in the vicinity of the edge when the wedge angle equals the tangent angle of the oncoming drop at the contact edge, and the impact speed of the oncoming wedge equals the drop impact speed. It is important to appreciate that during the crucial initial stage of impact the information that a collision has taken place is confined to the liquid region reached by the compression waves developed during the initial contact. This means that the collision with a large drop can be effectively studied by using a sector of liquid. As shown in Lesser (10) the pressure field is higher in the interior of a cylindrical or two-dimensional drop than a spherical drop, however, the edge behaviour is identical in both the two and three dimensional cases. Thus it becomes

reasonable to simplify the experimental study of the collision by using two-dimensional, preformed liquid shapes which are struck by a moving target. Techniques for impacting two-dimensional wedges of liquid were first described at the 1979 Erosion Conference (70). The further developments of this method are given in section 4.2 and new results in Sections 4.3 and 4.4.

4.2 EXPERIMENTAL

The idea of using disc-shaped bubbles or drops for cavitation of liquid impact studies was first suggested by Brunton (71). The technique was further developed in subsequent research (68, 69, 71-76). In the case of drop impact a small quantity of liquid was placed between two transparent plates separated by a small distance; surface tension pulled the liquid into a curved profile. Impact was achieved by projecting a third plate between the two spaced plates. High speed photography, using either a Bechman and Whitley (model 189) rotating mirror camera or single-shot schlieren photography, was used to record the impact events on a micro-second time scale. To obtain synchronization with the rotating mirror camera the impact plate was accelerated with an explosive detonator: the arrangements used achieved velocities of typically 100 m s^{-1} . (68, 69, 72). The great advantage of this two-dimensional work was that it allowed processes occurring inside an impacted drop to be observed in detail without the refraction problems inherent with spherical drops.

In their extension of this work Rochester and Brunton (73-76) fired an instrumented bullet (simulated target) at a two-dimensional drop and the impact pressure distribution was measured. The results showed that, although the "water hammer" pressure occurred at the centre, there were off-axis pressures of even greater magnitude and of roughly the size predicted by the theoretical work of Heymann (8) and Lesser (10).

A disadvantage of impact with a drop, both from the viewpoint of analysis and experimental interpretation, is that there is a constantly changing angle between the drop boundary and the solid (angle β in Figure 34). This is overcome by using wedges of liquid which have a constant, prechosen β .

In the present experiments two-dimensional wedges and other geometries were prepared by first mixing 12% by weight of gelatine with water, allowing it to set into a thin sheet and then cutting into the required shape. Previous work in the laboratory (77, 78) had used a similar approach to produce large spherical drops of liquid of up to 10 mm diameter, and had shown that the flow properties were not significantly different to that of pure water once impact velocities exceeded a few metres per second.

The water/gelatine sheets were made by casting into a 200 x 200 x 3 mm vertical mould to reduce evaporation. Both liquid and mould were at 330 K. Each of the large mould faces had been lightly greased and covered with a thin plastic film. After slow cooling, to reduce shrinkage, the mould was disassembled and the sheets placed horizontally. The layers, with plastic sheets attached, could be kept for several days. After some practice it was possible to cut out wedges with flat and smooth edges.

In early experiments, the chosen liquid/gelatine layer was placed between two thick, spaced glass blocks and mounted vertically in a frame. The impacting solid was a steel plate which was inserted between the glass plates to within 5 mm of the liquid wedge and with its rear surface projecting out from the blocks. The steel plate could be moved at velocities up to ca. 100 m s^{-1} by impacting with a plastic cylinder fired with velocities up to about 500 m s^{-1} from a 25 mm diameter bore gas gun. The steel plate triggered an Imacon framing image converter camera by intersecting a laser beam just before impact. A schematic diagram of the apparatus is shown in Figure 35. Schlieren optics were used to make the stress waves visible.

The basic problem with low impact velocities of less than 100 m s^{-1} is that the angle β for supersonic behaviour has to be less than ca. 3° . Producing controlled impacts with such small angles is difficult, and there are also problems in taking measurements from such sequences. Ideally velocities of a few hundred metres per second would be better since this would increase the angle β . A second experimental arrangement was therefore tried with a two-dimensional rectangular-bore gas gun

used to project the striker directly between the glass plates. This arrangement eliminated the need for separate strikers and projectiles as used in the first experiment. Having a rectangular bore gun barrel and incorporating the sabot and striker into one projectile gave sufficient control to be able to shoot the striker accurately between the glass plates and make it possible to achieve velocities of up to 150 m/s². This increased the angle to a rigid target, to ca. 4 degrees. The schlieren optics were improved by replacing the lenses of the former system with mirrors.

4.3 RESULTS

4.3a Wedge Impact

Figure 36 gives the impact geometry for a target striking a wedge of liquid. If U_i is the impact velocity, U_e the contact edge velocity and C the sound speed in the liquid, then we can relate the Mach numbers $M_i = U_i / C$ and $M_e = U_e / C$ by the equation $M_i = M_e \tan \beta$. Two situations can be distinguished, a supersonic contact point $M_e > 1$ (Figure 36a) and a subsonic contact point $M_e < 1$ (Figure 36b). The critical angle β_C below which the contact point is supersonic is when $M_e = 1$. For $M_i = 0.1$, β_C equals ca. 6°.*

* Please note that the theory in this report, including that given later for jetting, is linearized so that higher order terms in M_i are neglected. This means that C is taken as the acoustic wave speed. If a shock correction had been included it would have decreased β_C . At $M_i = 0.1$ the decrease is ca. 1°. Also neglected is the small amount of target movement during the high pressure impact phase. This gives a very small correction to β_C , which can be neglected here. However, as emphasized in Reference 82, its inclusion in the full theory of liquid impact is essential since it removes the stress singularity when the wave envelope is about to pass ahead of the contact point.

Figure 36 illustrates schematically the different predicted for the two situations. In case (a), the shock should be attached to the contact point with the shock envelope elongated in the x -direction and with no jetting in the wedge. In case (b) the primary shock should be part of a circle, with the shock ahead of the contact point and a jet forming.

Figures 37, 38 and 39 are all for an impact velocity of 150 m s^{-1} (i.e. $M_i = 0.1$) and with wedge angles of 3° , 6° and 12° respectively. They confirm all the predictions of the above model. In Figure 37, with a β value less than β_C , a strong shock envelope develops which expands much faster in the x -direction than vertically. No jet can be detected in the air wedge though a high speed jet, labelled J, of velocity ca. 2000 m s^{-1} forms when the shock envelope reflects at the right hand edge. Jet formation at the right hand edge is expected and is discussed in detail in the next section. Note that the reflected shock wave, S, now a wave of tension, causes cavitation in the liquid evident as the dark region labelled T.

Fig. 37. Impact with a wedge with β ca. 3° and $M_i = 0.1$. There is a supersonic contact point and no jetting in the wedge. A jet, labelled J, forms only when the shock reaches the left-hand boundary. The jet velocity is ca. 2000 m s^{-1} . Careful inspection of frame 5 shows an associated air shock. The dark region labelled T is due to cavitation.

Figure 38 is for $\beta = 6 \pm 0.5^\circ$ and is very close to the critical angle. Again, jet formation only occurs when the shock reaches the far boundary. A stronger shock would be predicted since β is closer to β_C (Reference 70) and support for this is that the velocity of the jet, labelled J, is ca. 2500 m s^{-1} which is higher than that in Figure 37.

In Figure 39, β is greater than β_C . The primary wave is now part of a circle, it moves ahead of the contact point and a jet can be detected in the air wedge from frame 4 onwards. The jet velocity in this case was ca. 1000 m s^{-1} .

4.3b Compliant Targets

Several authors have noted that jetting appears to start from under drops at values of β greater than that predicted by theory. For example, Camus (69) recorded angles between 10° and 20° with an average of 11° in the velocity range 30 to 100 m s^{-1} for impacts of a PMMA slider with a two-dimensional drop. Hancoc and Brunton (79) showed an angle of ca. 17° for impact at 80 m s^{-1} from damage studies on PMMA with their wheel and jet apparatus.

Various ideas have been advanced to explain this. An early suggestion by Hancoc and Brunton (79) that viscosity delays the onset of jetting is not convincing considering the velocities and pressures involved. Recently Lesser (10) has suggested that the compliance of the target has a major effect on increasing β_c , and experimental support for this is given below. Another factor likely to affect experimental observations is aerodynamic distortion of the contact surface of the drop to a greater effective radius. Finally, if the flow angle is deduced indirectly from damage studies the result will be an overestimate. The reasons for this are that when the jet first forms it may be too thin to have damage potential and further it needs to act on a perturbed surface. As Blowers (81) has shown, the Rayleigh surface wave which gives the main component of the surface displacements takes some time to reach a peak after the supersonic contact phase ceases.

We have begun to test Lesser's suggestion by firing compliant targets of molybdenum filled nylon. Figure 40 is an example with a value of 7.5° and an impact velocity of 180 m s^{-1} ($M_i = 0.12$). The contact edge clearly moves supersonically and there is no jetting inside the air wedge. We have also recorded a sequence for a compliant target at $M_i = 0.12$ and $\beta = 15^\circ$ in which there was jetting. The value of the critical angle β_c for a rigid target impacted at $M_i = 0.12$ is 6.8° . All we can say at present is that the experimental value for β_c lies in the range 7.5 to 15° . There seems, therefore, to be some support for the Lesser suggestion, but whether or not it is the main factor will need more experimental data. Further work is in progress.

4.4 JET VELOCITY

4.4a Theoretical

Earlier theoretical calculations for the impact of two-dimensional slugs of liquid were given in (70, 80). Here we extend this work to the geometry depicted in Figure 41. Impact first occurs at O and two wedge angles, α_1 and α_2 , are involved, both of which can be varied. However, the angle α_2 is kept below the critical angle so that the contact point moves supersonically along OA. The angle β can take values from the critical angle up to 90° . Of particular interest is the velocity of the jet after the target reaches point A.

Figure 42 illustrates schematically the situation when the target surface has passed point B. It shows the position of the shock envelope, the corner waves from the points O and A, the motion of the side wall at the left and the onset of jetting in the wedge.

The region labelled 1 in Figure 42 is redrawn in Figure 10, together with the image region 1'. The perturbed pressures on AB and BT are zero while over CT it is p_s . The pressure inside the enclosed region has been solved using conformal mapping techniques. As pointed out earlier it is important to note that the theory, as developed here, is a linear one, which applies only for small Mach numbers. It neglects shock effects and assumes C is the acoustic wave speed.

The aim is to calculate pressure and density variations in the regions behind the wavefronts from which jet velocities can be determined. In these regions, it is considered that the pressure and density are perturbed from their ambient values at atmospheric pressure. Insertion of the perturbed pressure, P and density, ρ into the equations of motion yields the 'acoustic' form of the equations governing the variations in the perturbed quantities.

$$\frac{\partial^2 \rho}{\partial t^2} - C^2 \nabla^2 \rho = 0 \quad 4.1$$

and

$$\frac{\partial^2 P}{\partial t^2} - C^2 \nabla^2 P = 0 \quad 4.2$$

where P and ρ are normalised by the water-hammer pressure, $P_w = \rho_0 C^2 V$ and the ambient density, ρ_0 , respectively.

Figure 43 shows the region marked 1 in Figure 4. The diagram shows the corner wave from the transition point A where the contact angle changes from β_0 to β . This mathematical model considers the pressure and density variations in region 1 defined by the corner wave, the free surface AB and the rigid target surface AC. It is the movement of the surface AB which produces the jetting outflow.

The first step is to determine the pressure in region 1 which gives the boundary condition along the corner wavefront. This is given by

$$P = P_s = \frac{M_e}{\sqrt{M_e^2 - 1}}$$

where M_e is the Mach number of the supersonic contact edge along AC and is given by

$$M_e = M_i / \tan \beta_0 \quad (10, 11, 70)$$

The wave equation (1) for the density may then be solved by a process of substitution. The first stage of substitution is of the form $\tilde{r} = r/a_0 t$ which removes the explicit time dependence to give a differential equation in \tilde{r} and θ . r and θ are polar co-ordinates with the transition point A as origin. By a further substitution of:

$$r = \frac{1 - \sqrt{(1 - \tilde{r}^2)}}{\tilde{r}} \quad (\text{Tschaplygin transformation})$$

this differential equation reduces to Laplace's equation:-

$$\frac{\partial^2 \delta(\tilde{r}, \theta)}{\partial \tilde{r}^2} = 0$$

and

$$\frac{\partial^2 \tilde{p}(\tilde{r}, \theta)}{\partial \tilde{r}^2} = 0$$

where \tilde{p} and $\tilde{\delta}$ are the normalised pressure and density, respectively in the new co-ordinate frame (\tilde{r}, θ) . \tilde{p} and $\tilde{\delta}$ may now be calculated using complex variable techniques (see Appendix A) and the results can be transformed back into the physically meaningful space (r, θ) to yield the pressure and density fields. From the pressure gradient normal to AC, the velocity of the liquid surface as it is forced from its original profile to start a jet, can be calculated.

Selected results are shown in Figure 44. In the cases illustrated M_i was 0.1 corresponding to an impact velocity of 150 m s^{-1} . At this velocity the critical angle is 5.71° . The x-component of the velocities, V_x , are given non-dimensionally in terms of C . R is also non-dimensional with the values 0 and 1 corresponding to the points A and B on the wedge surface (see Figure 42). Each figure contains three curves for different values of β_0 . The following general trend emerges: for a given β , the jet velocity increases as β_0 approaches the critical angle. The increase is particularly pronounced as β_0 is approached (note the changes as β_0 varies from 5.3 to 5.5 to 5.7°).

It is important to appreciate that the initial movement of the free surface reached by the shock is at right angles to AB. One consequence of this is that for angles of β , other than 90° , the moving liquid approaches the target surface at an angle and rebounds from it. This is certainly consistent with experimental observations which show the jet lifting up from the target surface. For small values of β the interaction between rebounding and incident liquid will be complex and the jet will quickly break up into a spray.

The results of Figure 44 for the x-component of the velocity do not give the jet velocity directly. This has to be obtained by integration. The surface begins to move when the shock wave reaches it (point B, and R value equal to 1.0). It will move with increased velocity as the target surface approaches and its R value decreases to 0. The area under the velocity/ R curve is the mean velocity which equals the jet velocity, V_j . Tables 1-3 summarize the predicted jet velocities for a range of configurations.

TABLE 4.1

Data for $\beta = 45^\circ$ and β_0 varied for $M_i = 0.1$, where $\beta_c = 5.71^\circ$.

β/\circ	β_0/\circ	Mean V_x/C	Mean $V_x = V_j / \text{m s}^{-1}$
45	1	0.056	80
45	3	0.086	130
45	5	0.182	270
45	5.3	0.236	350
45	5.5	0.326	490
45	5.7	1.44	2160

TABLE 4.2

Data for $\beta = 90^\circ$ and β_0 varied for $M_i = 0.1$, where $\beta_c = 5.71^\circ$

β/\circ	β_0/\circ	Mean V_x/C	Mean $V_x = V_j/m s^{-1}$
40	1	0.012	150
40	3	0.117	150
90	5	0.207	310
90	5.3	0.268	400
90	5.5	0.371	560
90	5.7	1.64	2460

TABLE 4.3

Data for various β with β_0 kept constant for $M_i = 0.1$, where $\beta_c = 5.71^\circ$

β/\circ	β_0/\circ	Mean V_x/C	Mean $V_x = V_j/m s^{-1}$
10	5.7	0.396	590
20	5.7	0.758	1140
30	5.7	1.07	1610
40	5.7	1.34	2010
50	5.7	1.53	2300
60	5.7	1.66	2490
70	5.7	1.72	2580
80	5.7	1.71	2570
90	5.7	1.64	2460

4.4b Experimental

Figure 45 gives an example of a double wedge with $\beta = 45^\circ$ and β_0 just sub-critical. A jet starts to form in frame 2. Its velocity, averaged between frames 2 and 8, is $600 \pm 100 m s^{-1}$. This agrees reasonably with the theoretical predictions (Table 1). It is difficult to be more precise since the jet velocity depends so critically on the value of β_0 in the range 5.3° to 5.7° .

We are also able to compare the results from Figures 37 and 38 with the theoretical predictions. Here the wedge angles were sub-critical and a jet only formed when the shock interacted with the right-hand boundary (i.e. $\beta = 90^\circ$). In Figure 37 β was ca. 3° and a jet velocity of ca. $2000 m s^{-1}$ was observed.

In Figure 38, β was $6 \pm 0.5^\circ$ and a jet velocity of ca. 2500 m s^{-1} was recorded. Comparison with the data of Table 2 shows that the second of these results is in excellent agreement. However, the jet velocity recorded for the 3° wedges is far higher than predicted. The explanation for this is that as the right-hand boundary is approached the wedge angle increases. (i.e. for example, it is curved up to ca 5° this would sharpen the shock and give the higher jet velocity. It emphasises how critical the pressures and jet velocities are to small changes in contact angle.

4.5 CONCLUSION

The two dimensional wedge impact configuration first described at the last ELSI Conference (1) has been significantly improved. Impact velocities up to 250 m s^{-1} are now attainable for both metal and plastic sliders (targets). It has been possible to photograph a variety of impact configurations and to compare the predicted shock structures and jet velocities.

It has been shown that it is possible to treat analytically the problem of jet flow from under a double wedge, where the first angle is sub-critical. In cases where it has been possible to compare theoretical prediction with experiment the agreement has been good. Further work is planned.

The results emphasise how critical the detailed shape of the liquid/solid interface is in the region of contact. If the contact angle is less than β_c then high pressures are associated with the contact point, but there is no jetting. If β is greater than β_c then the pressures are less, the wave passes ahead of the contact point and jet flow commences.

The present work has clarified the conditions under which jetting occurs and also predicts the likely jet velocities. As also pointed out in reference 82, the initial movement of the liquid surface is at right angles to the liquid surface. Thus, in cases where β is $< 90^\circ$, the liquid has a component towards the target surface.

The geometries discussed in this paper have relevance to liquid impact, explosives welding and jet production from a shaped-charge.

APPENDIX

After transformation to the $(\tilde{r}, \tilde{\theta})$ plane, the problem reduces to a boundary value one on the upper half of the unit circle for $\tilde{p}(\tilde{r}, \tilde{\theta})$. As $\nabla^2 \tilde{p}(\tilde{r}, \tilde{\theta}) = 0$, this is most easily solved by complex variable techniques. The region (1) and its boundary conditions are shown in Figure 43. The boundary condition along AC is $\tilde{p} \cdot \tilde{n} = 0$ and this may be dealt with by the method of images so that now pressures are known on all boundaries. The reflected sector is also shown in Figure 43.

Regions 1 and 1' are then mapped into the upper half of the plane by transformation.

$$z = \frac{(e^{iz} - z)^{-1/2} (\pi - \tilde{\beta}) + 1}{(e^{-iz} - z)^{-1/2} (\pi - \tilde{\beta}) - 1}$$

A unique solution satisfying the appropriate boundary condition is:

$$P = \text{Real Part } \left\{ P_s \frac{i}{\pi} \ln \frac{z + u}{z + v} \right\}$$

$$\text{where } P_s = \frac{M_e}{\sqrt{(M_e^2 - 1)}}$$

$$u = \cot^2 \left\{ \frac{\pi}{4} \left[\frac{\lambda_o - \tilde{\beta}}{\pi - \tilde{\beta}} \right] \right\}$$

$$v' = \cot^2 \left\{ \frac{\pi}{4} \left[\frac{2\pi - \lambda_o - \tilde{\beta}}{\pi - \tilde{\beta}} \right] \right\}$$

$$\tan \lambda_o = \sqrt{(M_e^2 - 1)}$$

$$M_e = M_i / \tan \beta_o$$

where β_o is the first contact angle for which the contact edge is supersonic. Transforming back into the $\tilde{r}, \tilde{\theta}$ place leads to formulae for \tilde{p} and $\tilde{\beta}$ from which the pressures p and σ can be derived as described earlier.

REFERENCES

1. Field, J.E., Matthewson, M.J. and van der Zwaag, S., Annual Report 1979, AFOSR-78-00125.
2. Field, J.E., van der Zwaag, S. and Hagan, J.T., Annual Report 1981, AFWAL-TR-81-4026.
3. van der Zwaag, S. and Field, J.E., Annual Report 1981, AFWAL-TR-81-4022.
4. Field, J.E., Gorham, D.A., Hagan, J.T., Matthewson, M.J., Swain, M.V. and van der Zwaag, S., 1979, Proc. 5th Int. Conf. on Erosion by Solid and Liquid Impact (ed. J.E. Field), Paper 13, Cavendish Laboratory, Cambridge.
5. Brunton, J.H. and Rochester, M.C., 1979, "Erosion. Treatise on Materials Science", Vol. 16 (ed. C.M. Preece), Academic Press, New York.
6. Bowden, F.P. and Field, J.E., 1964, Proc. Roy. Soc. Lond. A282, 331.
7. Cook, S.S., 1928, Proc. Roy. Soc. Lond. A119, 481.
8. Heymann, F.J., 1969, J. Appl. Phys. 40, 5113.
9. Field, J.E., Lesser, M.B. and Davies, P.N.H., 1979, Proc. 5th Int. Conf. on Erosion by Liquid and Solid Impact, Cambridge.
10. Lesser, M.B., 1981, Proc. Roy. Soc. Lond. A377, 289.
11. Lesser, M.B. and Field, J.E., 1983, Ann. Rev. Fluid Mech. 15, 97.
12. Field, J.E., Gorham, D.A. and Rickerby, D.G., 1979, ASTM STP 664 (ed. W.F. Adler), p.298.
13. van der Zwaag, S. and Field, J.E., 1983, Engng. Fract. Mech. 17, 367.
14. Bowden, F.P. and Brunton, J.H., 1961, Proc. Roy. Soc. Lond. A263, 433.
15. Gorham, D.A. and Rickerby, D.G., 1974, J. Phys. E. 8, 794.
16. Matthewson, M.J. and Field, J.E., 1980, J. Phys. E. 13, 355.
17. Mecholski, J.J., Freiman, S.W. and Rice R.W., 1976, J. Mater. Sci. 11, 1310.
18. van der Zwaag, S. and Field, J.E., 1982, J. Mater. Sci. 17, 2625.
19. Swain, M.V. and Hagan, J.T., 1980, J. Mater. Sci. 15, 387.
20. Eshelby, J.D., 1970, "Inelastic Behaviour of Solids", (ed. M.F. Kanninen), McGraw Hill, New York.
21. Rose, L.F.R., 1976, Int. J. Fracture Mech. 12, 799.
22. Kerkhoff, F. and Richter, H., 1969, Proc. 2nd Int. Conf. on Fracture, Brighton.
23. A. de S. Jayatilaka and Trustum, K., 1977, J. Mater. Sci. 12, 1462.
24. Wiederhorn, S.W. and Lawn, B.R., 1977, J. Amer. Ceram. Soc. 60, 451.

25. Heymann, F.J., 1968, J. Basic. Eng. Trans. ASME D 90, 400.
26. Gutshall, P.L. and Gross, G.E., 1969, Eng. Fract. Mech. 1, 463.
27. Evans, A.G. and Tappin G. 1972, Proc. Brit. Ceram. Soc. 20, 275.
28. Swanson, G.D., 1972, J. Am. Cer. Soc. 55, 48.
29. Lynch, J.F. and Bradt, R.C., 1973, J. Am. Cer. Soc. 56, 228.
30. Pratt, P.L., 1977, Proc. Int. Conf. on Fracture, Waterloo, Canada, Vol. 3, p.909.
31. Rice, R.W., 1977, in "Treatise on Mat. Sci. and Tech": Vol. II, Academic Press, 241.
32. Veldkamp, J.D.B. and Hattu, N., 1979, Philips J. Res. 34, 1.
33. Simpson, L.A., 1973, J. Amer. Cer. Soc. 56, 7.
34. Simpson, L.A., 1973, ibid, 56, 610.
35. Lawn, B.R. and Fuller, E.R., 1975, J. Mater. Sci. 10, 20.
36. Hornbogen, E., 1975, Z. Metallk. 66, 511.
37. Kawatake, T. and Izumi, O., 1978, J. Mater. Sci. 13.
38. van der Zwaag S., Hagan, J.T. and Field, J.E. 1980, J. Mater. Sci. 15, 2695.
39. Swain, M.V. and Hagan, J.T., 1976, J. Phys. D: 9, 220.
40. Evans, A.G. and Wilshaw, T.R., 1976, Acta. Met. 27, 939.
41. Hagan, J.T., 1979, J. Mater. Sci. 14, 2975.
42. Hannink, R.S.J. and Swain, M.V., 1980, J. Mater. Sci. 16, 1428.
43. Nadai, A., 1931, "Plasticity", McGraw-Hill, New York.
44. van der Zwaag, S. and Field, J.E., 1982, Phil. Mag. 46, 133.
45. van der Zwaag, S. and Field, J.E., 1983, Phi. Mag. (in press).
46. Adler W.F., 1979, Report No. CR 79-611 (Effects Technology Inc. Santa Barbara, U.S.A.).
47. van der Zwaag, S. and Field, J.E., 1982, J. Mater. Sci. 17, 2625.
48. Marsh, K.J. and Savage, J.A., 1974, Infrared Phys. 14, 85.
49. Donald, J.W. and McMillan, P.W., 1978, J. Mater. Sci. 13, 1151.
50. Dick, E., 1970, Glastechn. Ber. 43, 16.
51. Lawn, B.R. and Evans, A.G., 1977, J. Mater. Sci. 12, 2195.
52. Chiang, S.S., Marshall, D.B. and Evans, A.G., 1982, J. Appl. Phys. 53, 298.
53. Chiang, S.S., Marshall, D.B. and Evans, A.F., 1982, J. Appl. Phys. 53, 311.
54. Hagan, J.T., and Swain, M.V., 1978, J. Phys. D. 11, 2091.
55. Hockey, B.J. and Wiederhorn, S.M. 1970, Proc. 5th Int. Conf. on Erosion by Liquid and Solid Impact, Cambridge, paper 26.

56. Banerjee, R.K. and Feltham, T., 1974, J. Mater. Sci. 9, 1478.
57. Lankford, J. and Davidson, D.L., 1974, J. Mater. Sci. 14, 1662.
58. Lawn, B.R. and Wilshaw, T.R., 1975, "Fracture of Brittle Solids", Cambridge University Press, Cambridge.
59. Hooker, S.V., 1977, Near, 43, 253.
60. Neffre, D., Ashby, M.F., Lawn, B.R. and Wilshaw, T.R., Acta. Met. 19, 779.
61. Testardi, L.R. and Hauser, J.J., 1977, Solid State Comm. 21, 103.
62. Blair, P.W., 1981, Ph.D. Thesis, University of Cambridge.
63. Hackworth, J.V., 1978, Ann. Report AMFL-TR-78-184, Bell Aerospace Textron, Buffalo, New York.
64. Brunton, J.H. and Rochester, M.C., 1979, "Erosion of Solid Surfaces by the Impact of Liquid Drops" in "Erosion", ed. C.M. Preece, Academic Press, New York, 185.
65. Adler, W.F. (ed.) 1979 "Erosion: prevention and useful applications" Philadelphia, Penn. ASTM.
66. Jenkins, D.C. and Booker, J.D., 1960, in "Aerodynamic Capture Particles" ed. E.G. Richardson, Pergamon, Oxford, pp.97.
67. Fyall, A.A., 1967, Proc. 2nd Int. Conf. on Rain Erosion and Associated Phenomenon, Meersburg, W. Germany, (eds. A.A.Fyall, R.B. King) RAE Farnborough, UK. p. 563.
68. Brunton, J.H. and Camus, J-J., 1970, Proc. 3rd Int. Conf. on Rain Erosion and Associated Phenomena, Meersburg, W. Germany (eds. A.A. Fyall and R.B. King), RAE Farnborough, U.K.
69. Camus, J-J., 1971, Ph.D. Thesis, University of Cambridge.
70. Field, J.E., Lesser, M.B. and Davies, P.N.H., Proc. 5th Int. Conf. on Erosion by Liquid and Solid Impact (ed. J.E. Field) Cambridge 1979.
71. Brunton, J.H., 1967, Proc. 2nd Int. Conf. on Rain Erosion and Allied Phenomena, Meersburg, W. Germany, (eds. A.A. Fyall and R.B. King), RAE Farnborough, U.K.
72. Brunton, J.H. and Camus, J-J., 1970, Proc. 9th Int. Conf. High-Speed Photog. (eds. W.G. Hyzer and W.G. Chase) SMPTE, New York, p.444.
73. Rochester, M.C. and Brunton, J.H., 1974, ASTM, Philadelphia, Penn. STP 567, p.128.
74. Rochester, M.C. and Brunton, J.H., 1974, Proc. 4th Int. Conf. on Rain Erosion and Associated Phenomena, Meersburg, W. Germany (eds. A.A. Fyall and R.B. King)RAE Farnborough, UK. p.371.

75. Rochester, M.C., 1979, Ph.D. Thesis, University of Cambridge.
76. Rochester, M.C. and Brunton, J.H., 1979, Proc. 5th Conf. on Erosion by Liquid and Solid Impact, (ed. J.E. Field), Cambridge, paper 6.
77. Rickerby, D.G., Ph.D. Thesis, University of Cambridge, 1977.
78. Field, J.E. Gorham, D.A. and Rickerby, D.G., 1979, In "Erosion : prevention and useful applications", ASTM, Philadelphia, Pa. STP 694, p. 298.
79. Hancox, N.L. and Brunton, J.H., 1966, Phil. Trans. Roy. Soc. Lond. A260, 121.
80. Lesser, M.B. and Field, J.E., 1974, Proc. 5th Int. Conf. on Rain Erosion and Allied Phenomena, Meersburg, W. Germany (eds. A.A. Fyall and R.B. King), RAE Farnborough, UK.
81. Blowers, R.M., 1969, J. Inst. Math. Applic. 5, 167.
82. Lesser, M.B. and Field, J.E., Proc. 6th Int. Conference on Erosion by Liquid and Solid Impact (eds. J.E. Field and N.S. Corney) Cambridge, Sept. 1983.

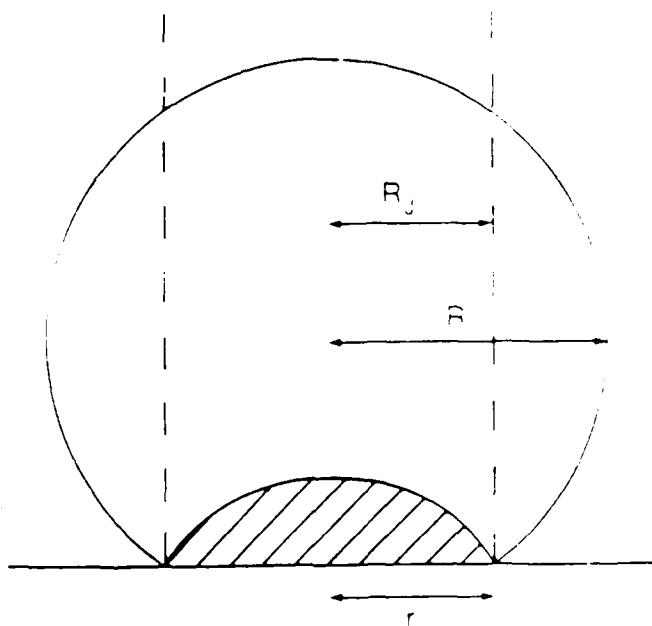


Fig. 1. Relation between jet radius, R_j , and impact radius, R_i . The shaded area represents schematically the compressed liquid which generates the high pressures.

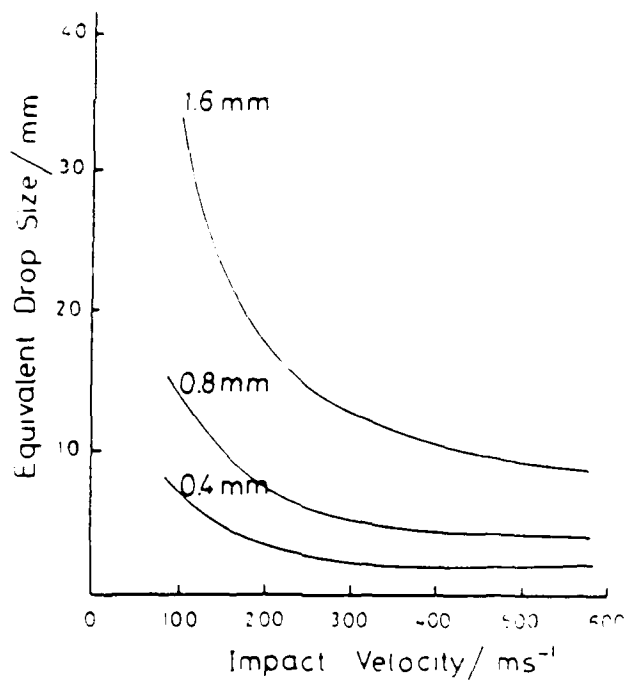
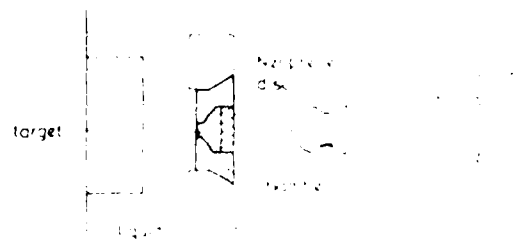


Fig. 2. Equivalent drop size as a function of impact velocity for jets of different sizes.



a



b

Fig. 3. Schematic of impact apparatus.

(a)

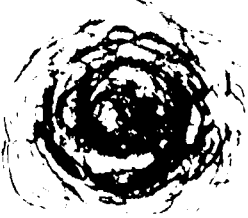
t'

1 mm

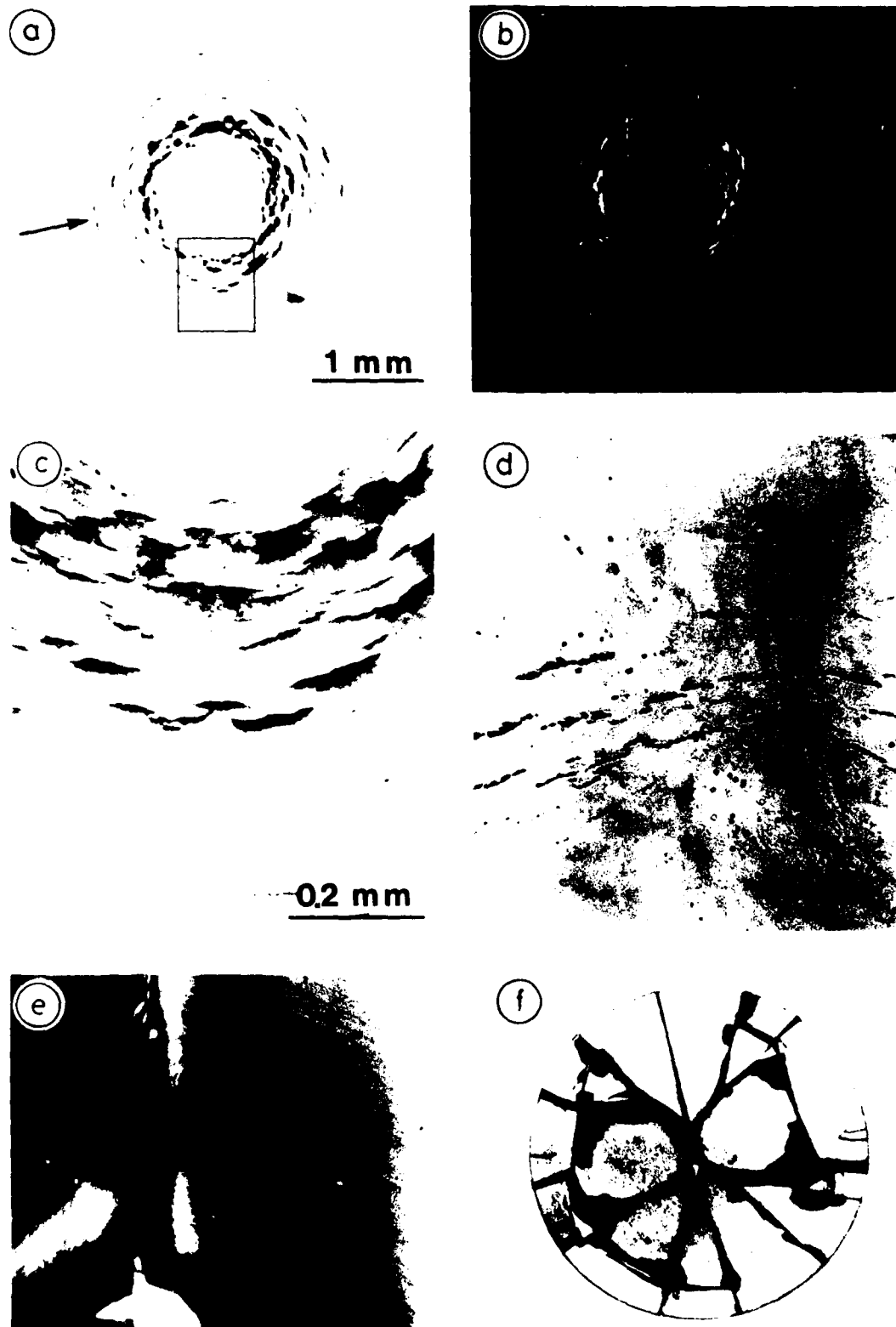
(b)



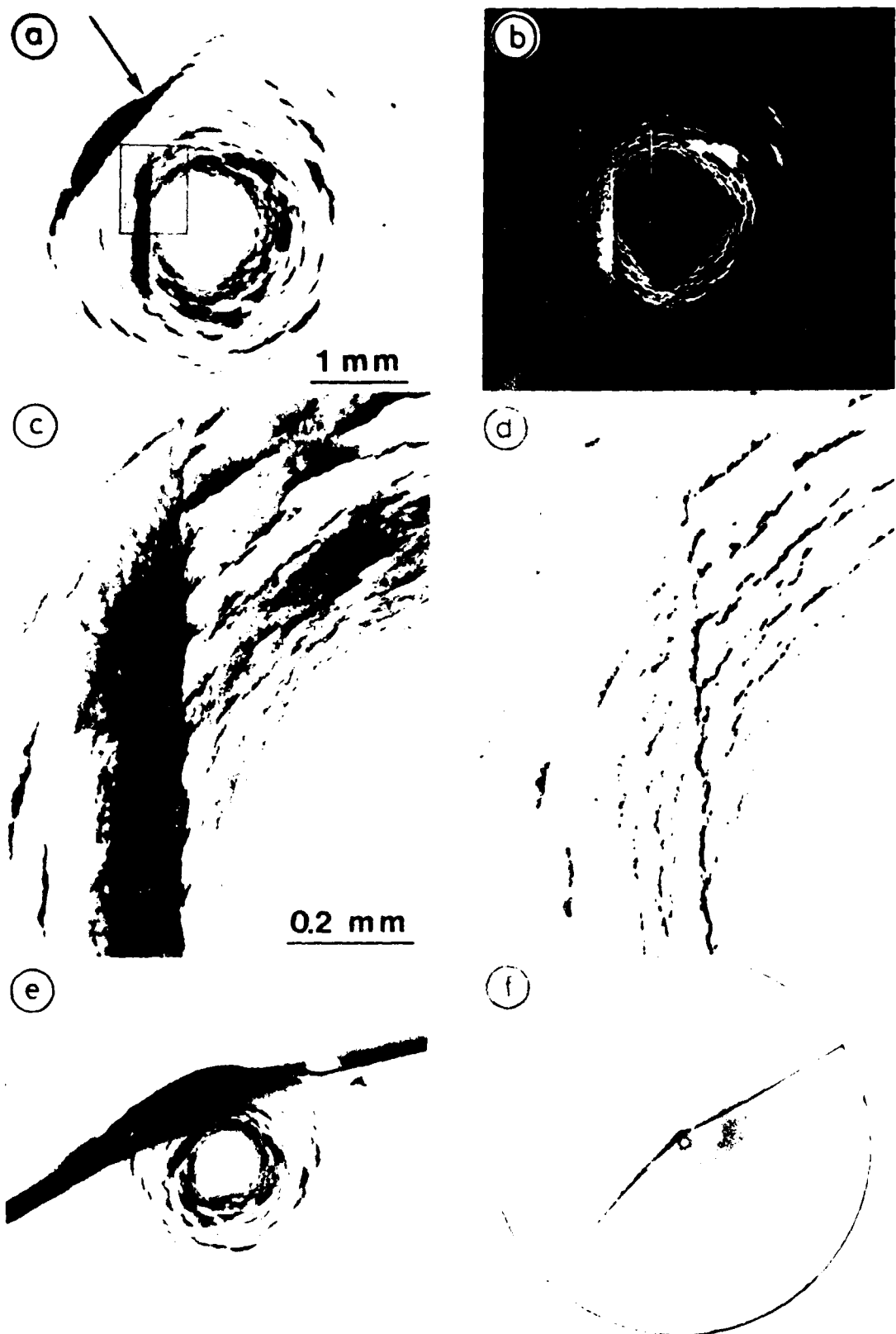
(c)



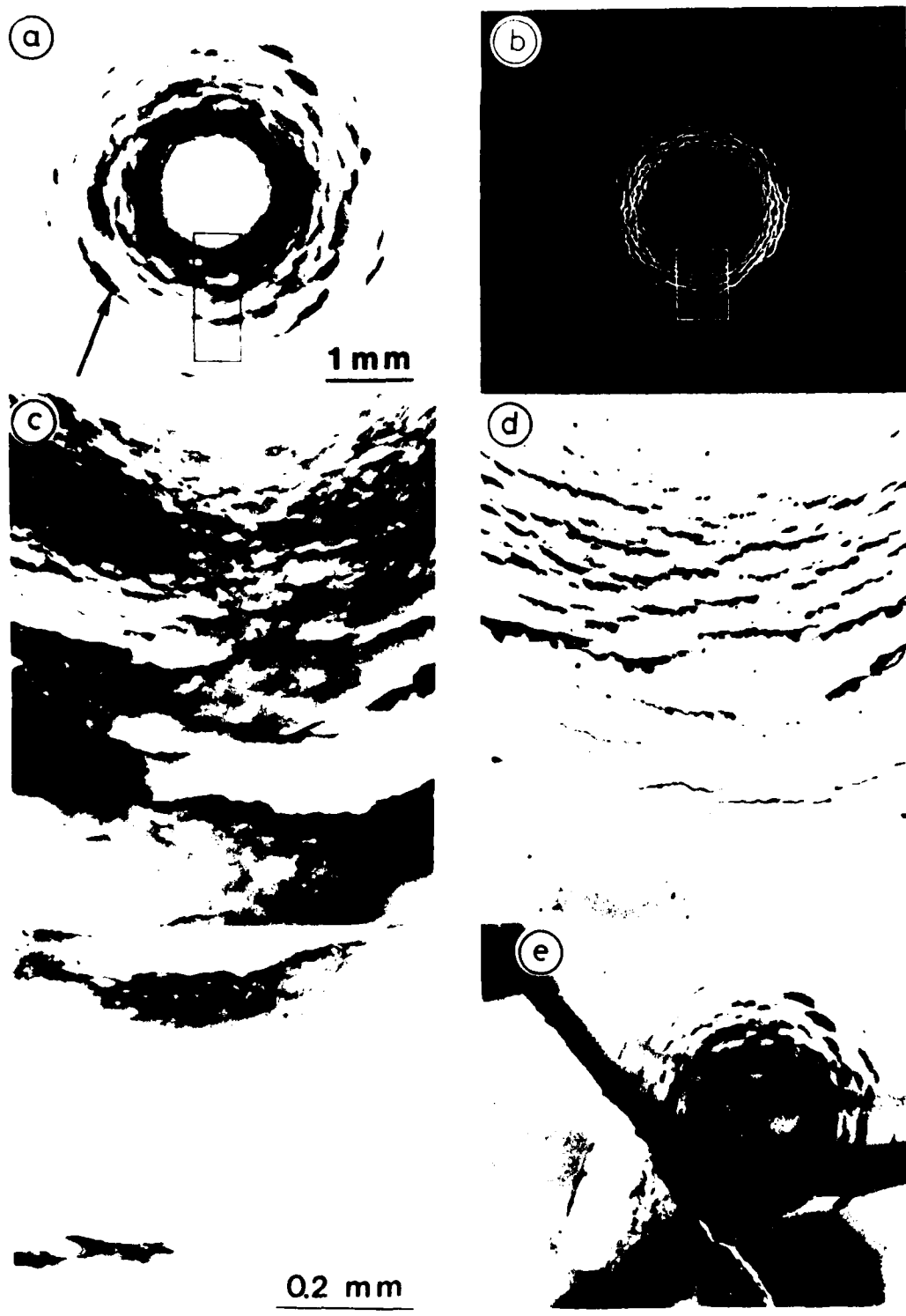
4. Examples of impact craters in fine glass due to jet impact at various angles. Equivalent to impacts with a velocity of impact of (a) 300 m s^{-1} , (b) 450 m s^{-1} , (c) 600 m s^{-1} .



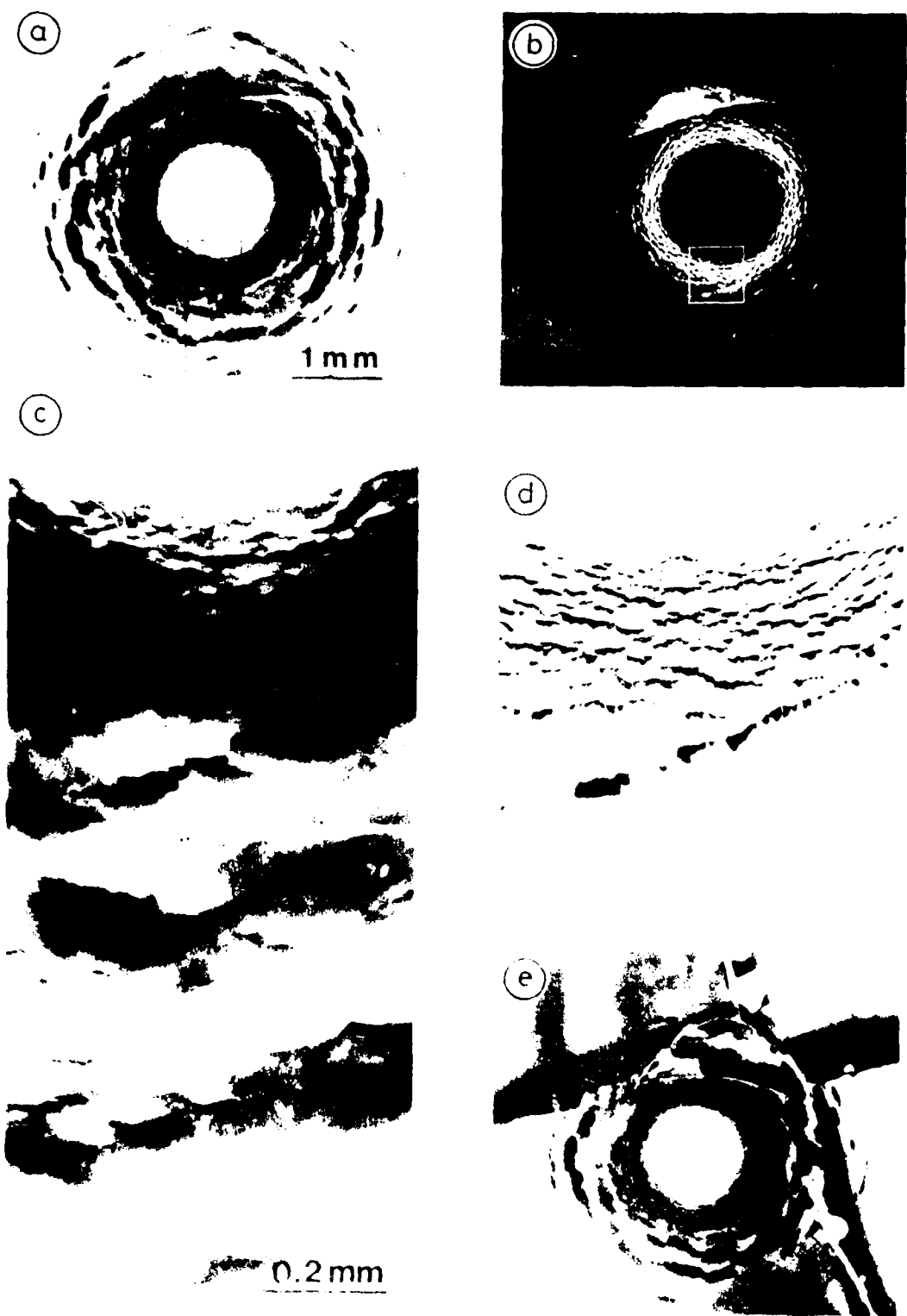
5. Micrographs obtained with a 0.8 mm jet impact at 175 m s^{-1} . (a) optical transmission micrograph of the impact damage. (The flaw leading to failure in the pressure tester is arrowed). (b) Micrograph with oblique reflective illumination; magnification as in (a). (c) and (d) enlargements of the areas marked in (a) and (b) respectively; magnification for (d) as in (c). (e) and (f) the specimen after failure in the pressure tester.



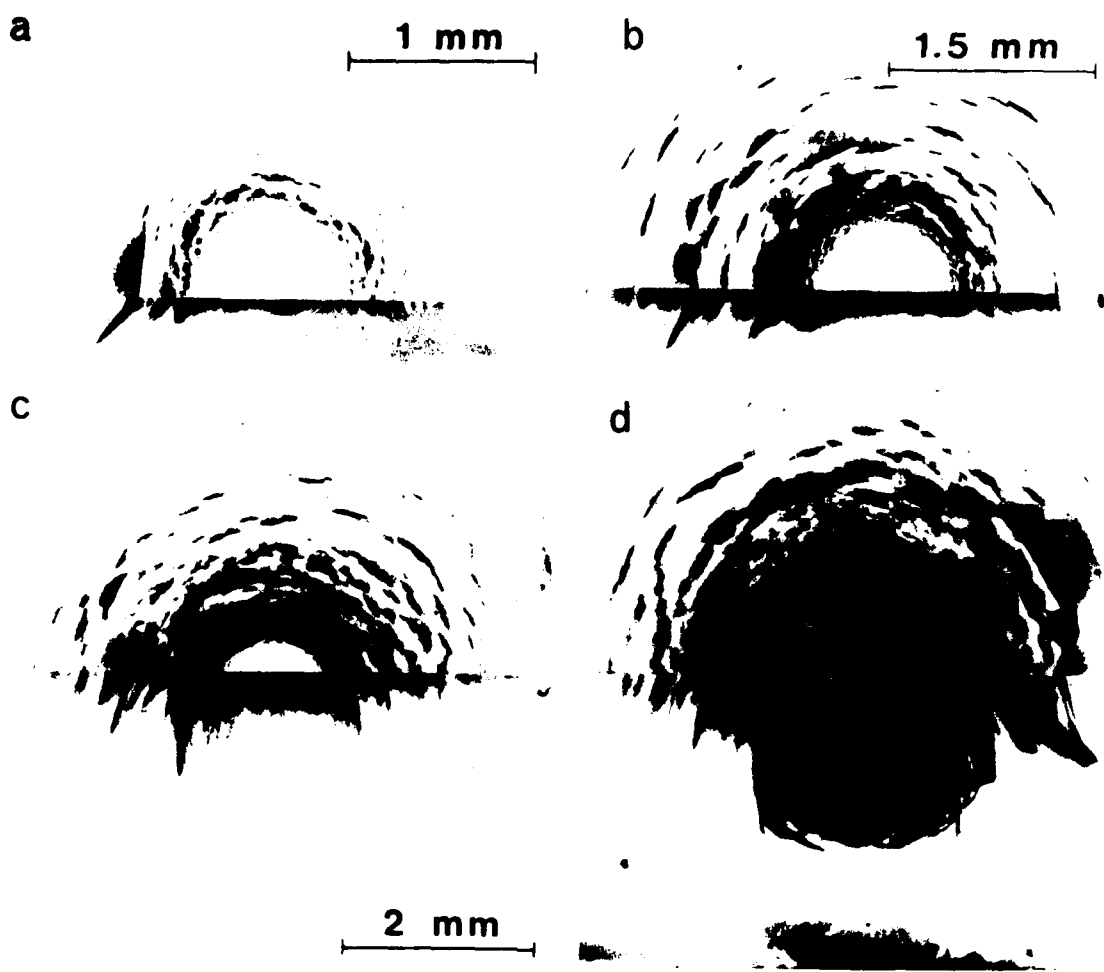
6. Micrographs obtained with a 0.8 mm jet impact at 200 m s^{-1} . (a) Optical transmission micrograph of the impact damage. (The flaw leading to failure in the pressure tester is arrowed). (b) Micrograph with oblique reflective illumination; magnification for (d) as in (c). (c) and (d) the specimen after failure in the pressure tester.



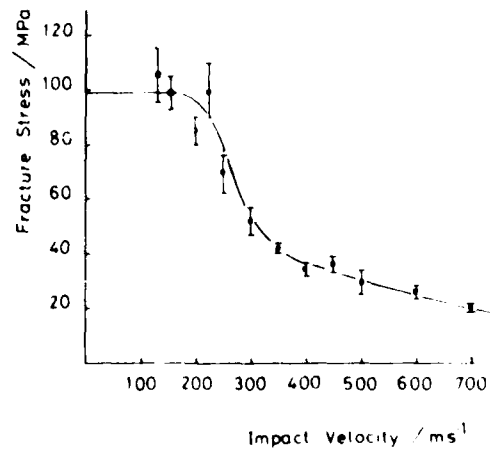
7. Micrographs obtained with a 0.8 mm jet impact at 300 m s^{-1} . (a) Optical transmission micrograph of the impact damage. (The flaw leading to failure in the pressure tester is arrowed). (b) Micrograph with oblique reflective illumination; magnification as in (c). (c) and (d) enlargements of the areas marked in (a) and (b) respectively; magnification for (d) as in (c). (e) and (f) the specimen after failure in the pressure tester.



8. Micrographs of the specimen after 1.5 mm jet impact at 500 m s^{-1} . (a) Optical transmission micrograph showing central damage. (The flaw leading to failure in the pressure tester is also shown.) (b) Enlargement with oblique reflective illumination; magnification $\times 10$. (c) (d) enlargements of the areas marked in (a) and (b) respectively; magnification $\times 10$. (e) (f) the specimen after failure in the pressure tester.



9. Cross-section of the 0.8 mm jet impact damage in zinc sulphide. (a) 170 m s^{-1} , (b) 300 m s^{-1} , (c) 400 m s^{-1} , (d) 600 m s^{-1} .



10. Variation of the residual fracture stress with jet impact velocity for soda-lime glass. Jet from 0.8 mm orifice. Error bars indicate standard deviation of the mean.

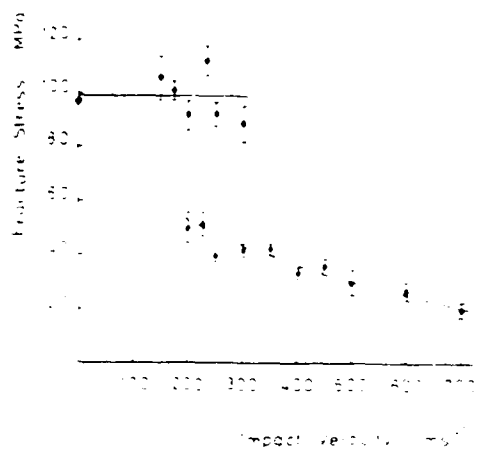


Fig. 11. Same data as in Fig. 10 but now results for "undamaged" and damaged specimens plotted separately.

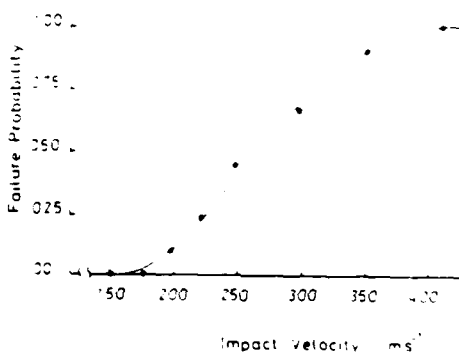


Fig. 12. Variation of failure probability with jet impact velocity. Same data as in Fig. 10. Estimated uncertainty $\pm 10\%$.

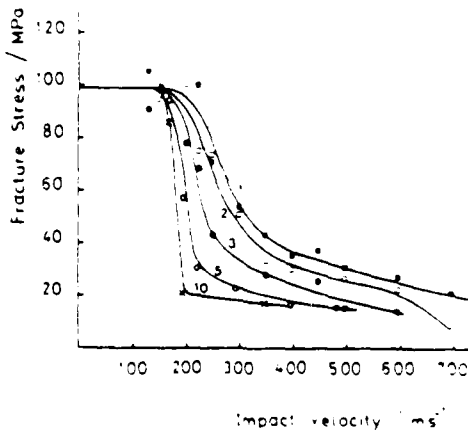
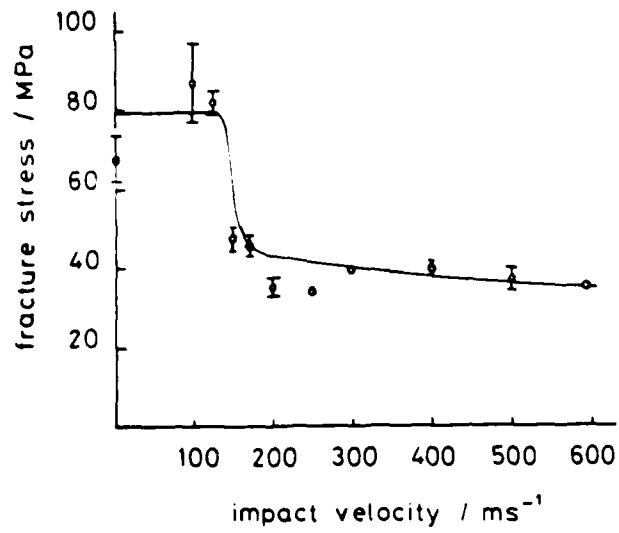
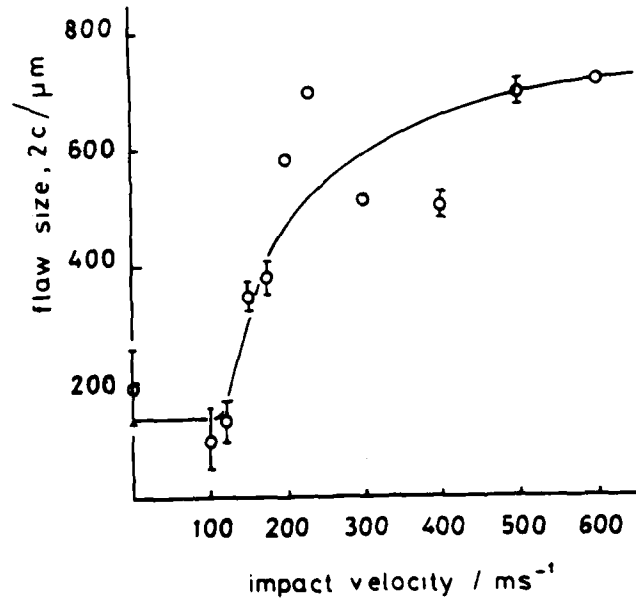


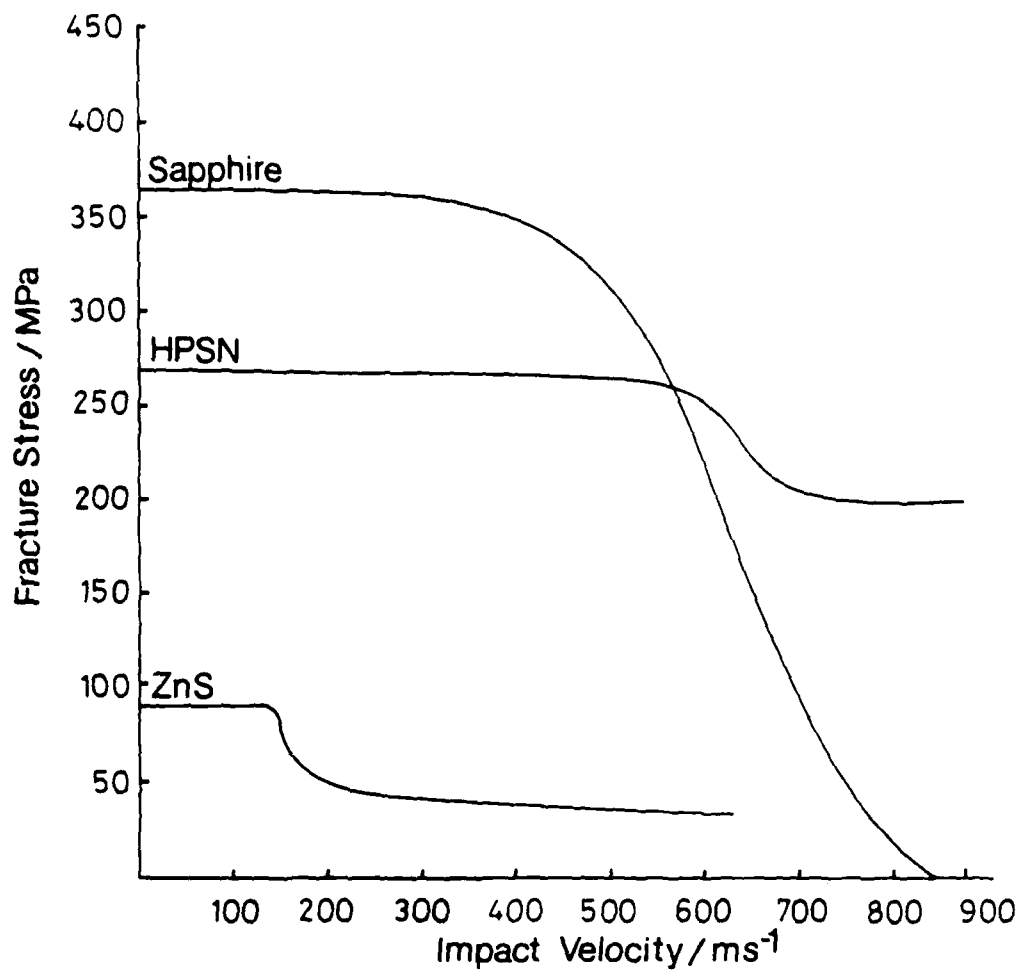
Fig. 13. Variation of residual fracture stress after single and multiple jet impact.



14. Residual strength curve for ZnS for single impact with jets from a 0.8 mm nozzle.



15. Equivalent flaw sizes for ZnS as a function of impact velocity.



16. Residual strength curves for ZnS, a hot-pressed silicon nitride and single crystal sapphire impacted on the basal plane.

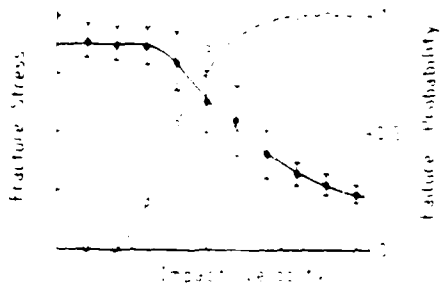


Fig. 17. Theoretical residual strength curve (—) and failure probability curve (---) for soda-lime glass (see text).

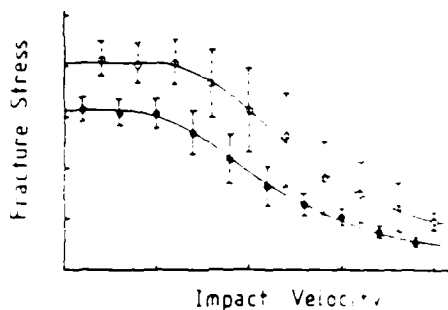


Fig. 18. Theoretical residual strength curves for soda-lime glass (see text). o "as received" specimens. ● "abraded" specimens.

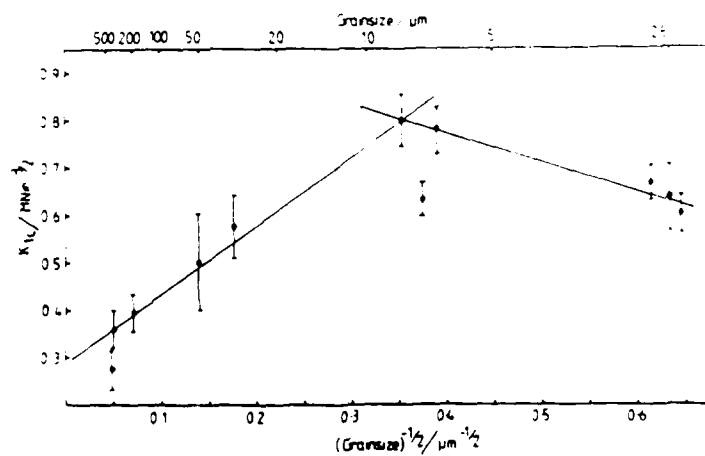
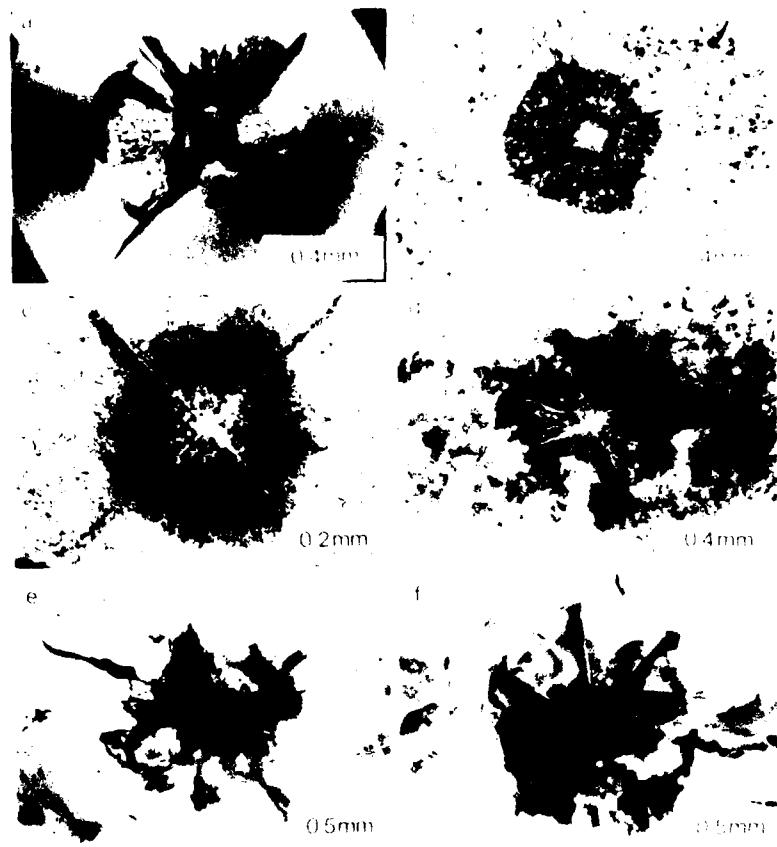
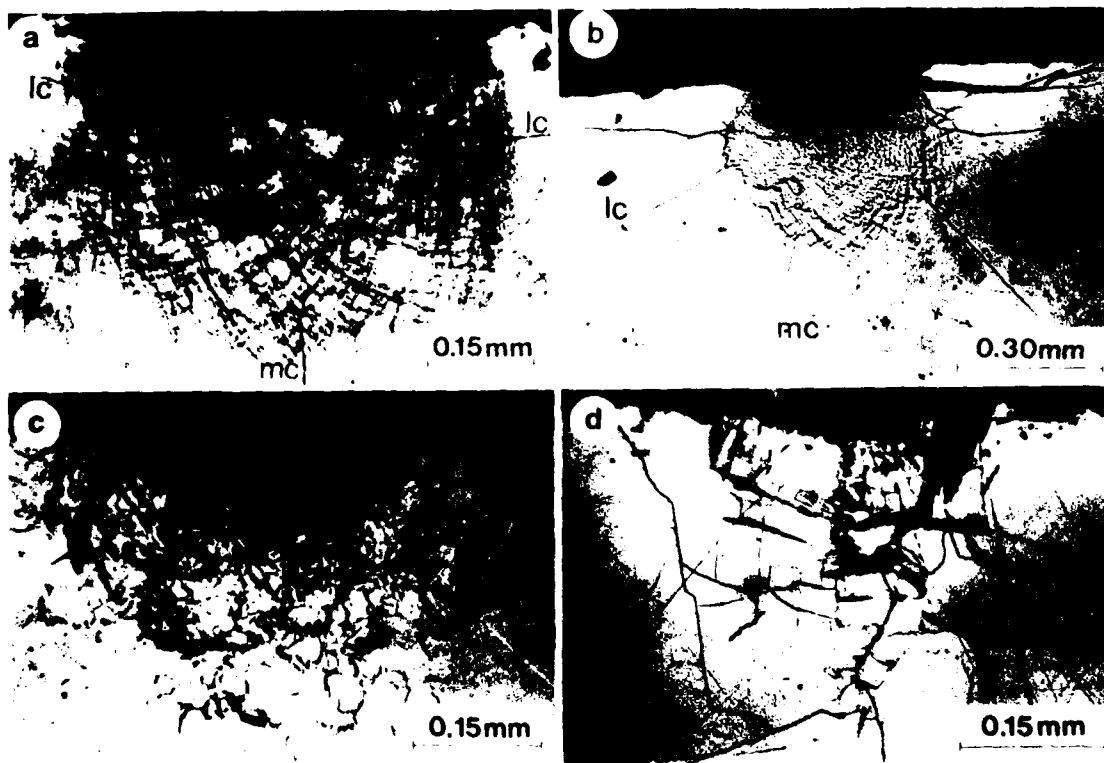


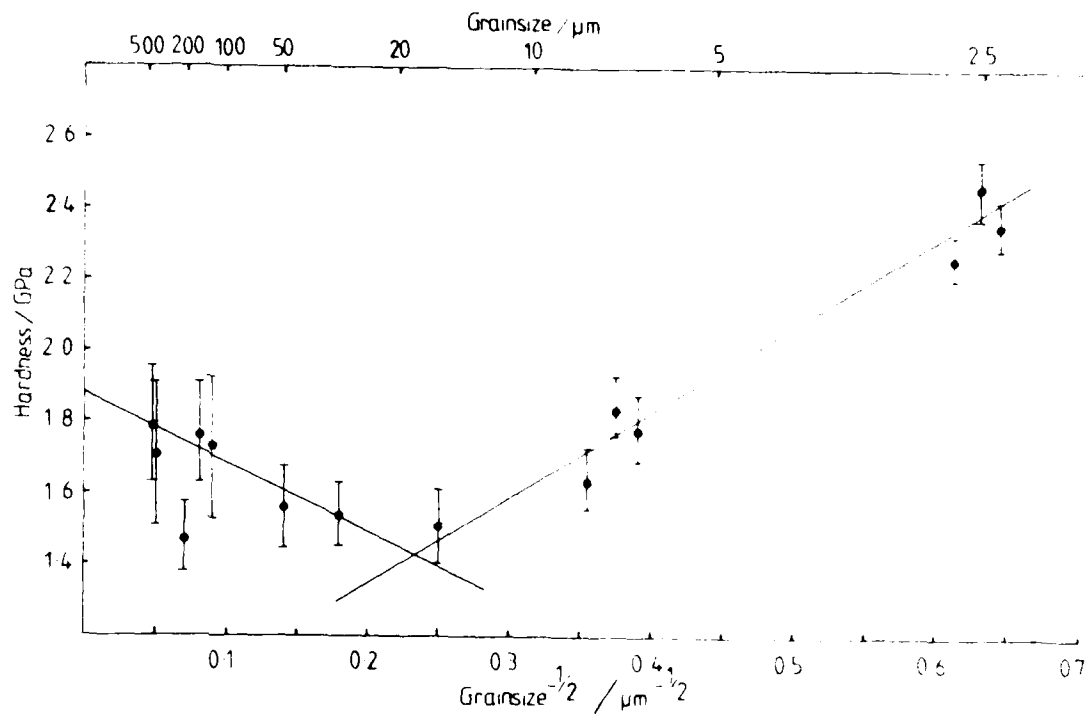
Fig. 19. K_{Ic} versus $(\text{grain size})^{-\frac{1}{2}}$ for ZnS.



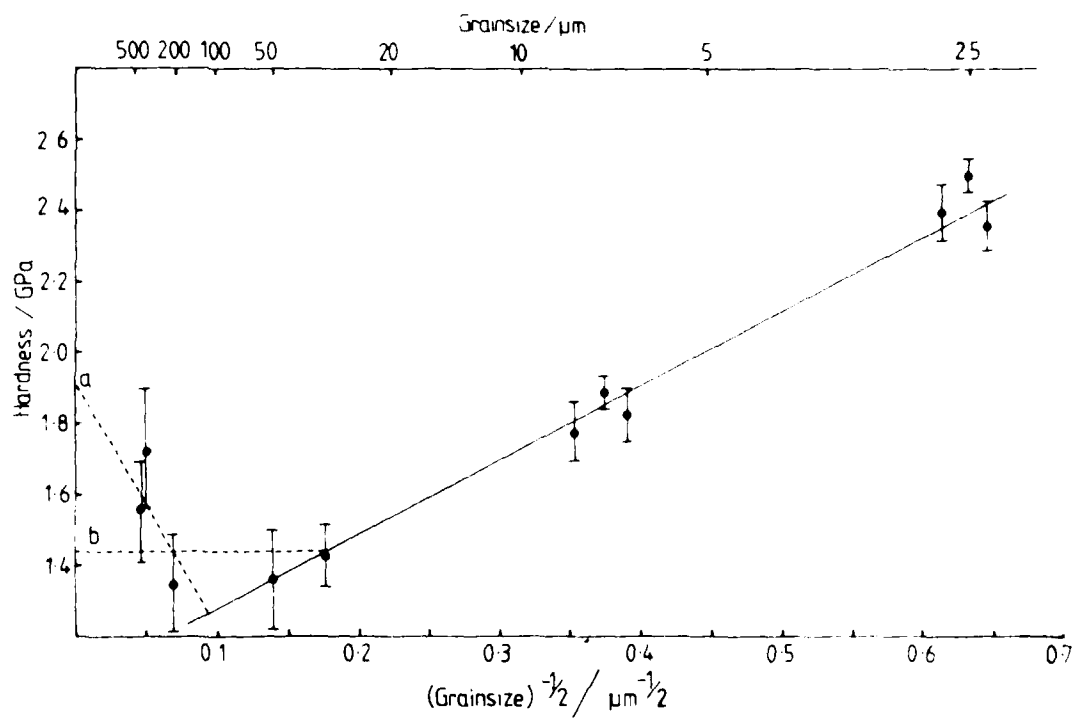
20. Surface views of Vickers indents on ZnS. All for loads of 100 N. (1) 2.5 μm grain size, (b) 6.5 μm , (c) 8 μm , (d) 32 μm (e) 140 μm and (f) 400 μm . See text for details.



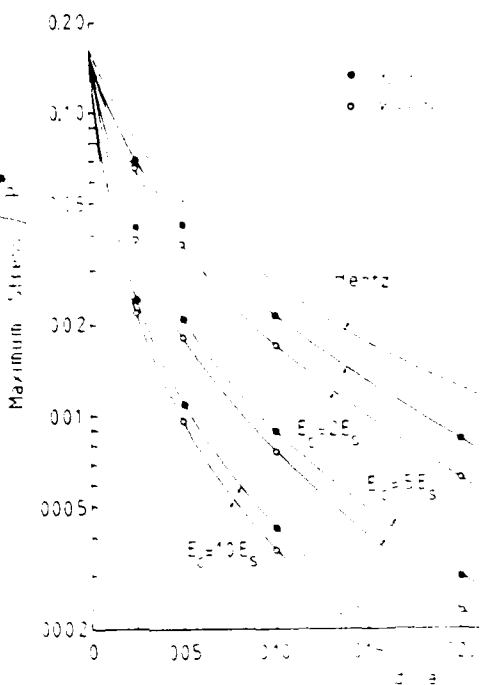
21. Grain dependence of the subsurface deformation mode for Vickers indentations on ZnS. (a) 300 N indentation for 0.5 μm grain size, (b) 75 N for 2 μm , (c) 150 N for 16 μm and (d) 100 N for 140 μm .



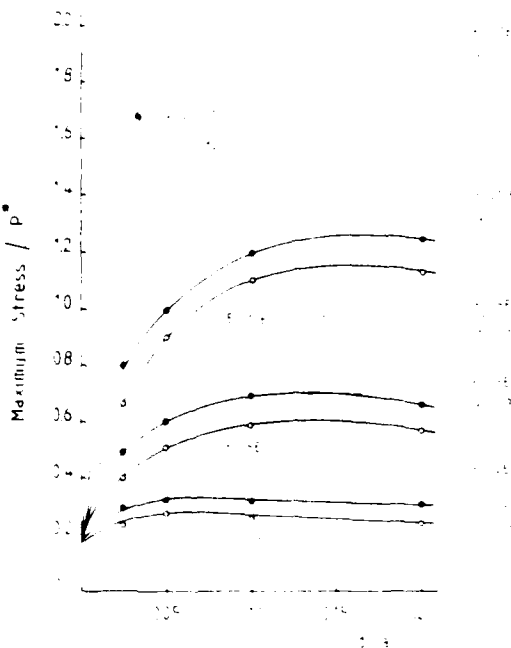
22. Vickers hardness versus $(\text{grain size})^{-\frac{1}{2}}$ for InS.
Indenter load 10 N.



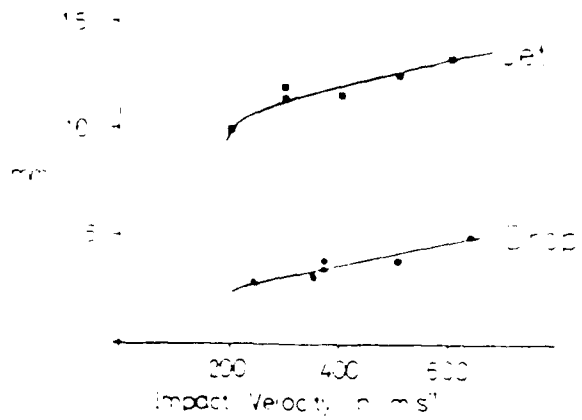
23. Vickers hardness versus $(\text{grain size})^{-\frac{1}{2}}$ for ZnS.
Indenter 10 + 100 N.



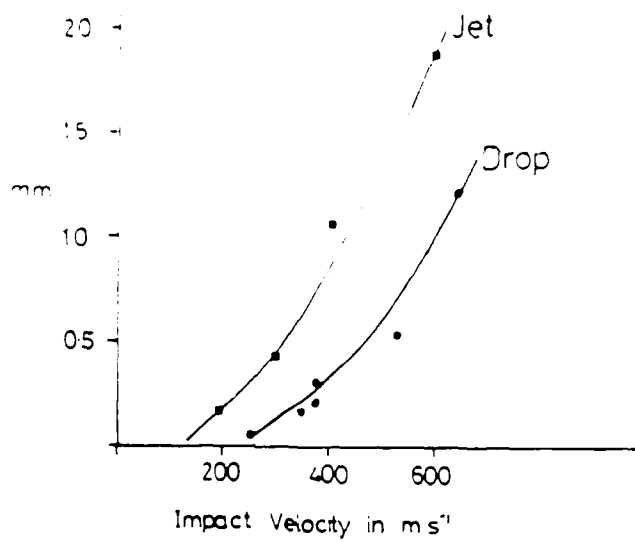
24. Variation of the maximum radial stress at the interface with the coating parameters. P^* is the maximum axial stress in the coating surface, d is the coating thickness and a the radius of the contact zone.



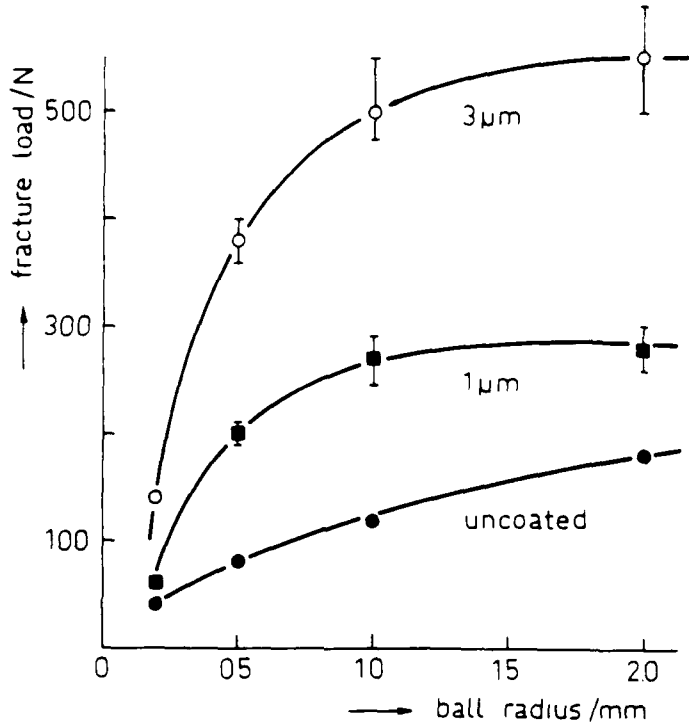
25. Variation of the maximum tensile stress at the coating surface with coating parameters. E_c and E_s are the Young's modulus of the coat and substrate respectively, ν is Poisson ratio. See reference 45 for further details.



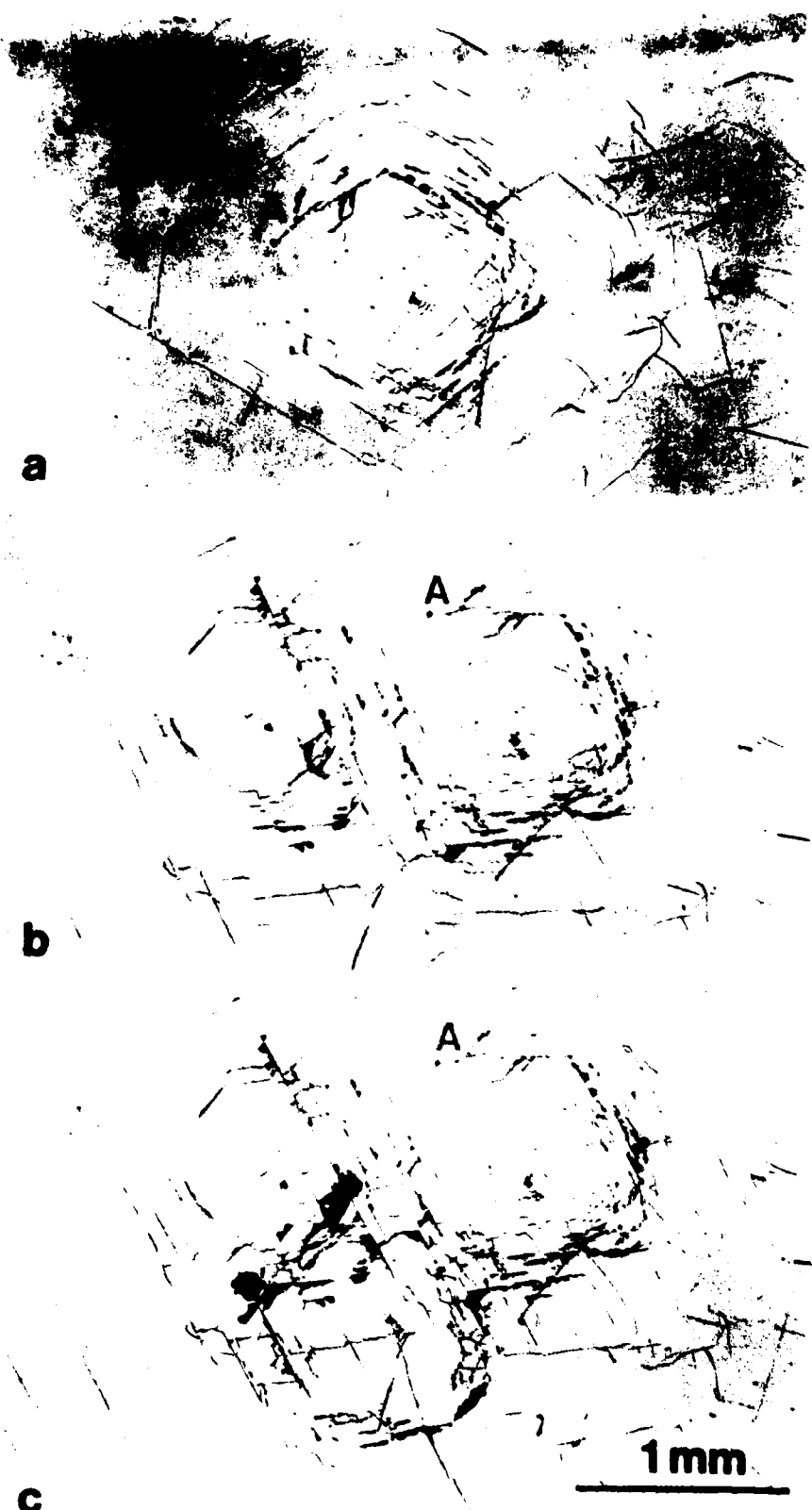
26. Velocity dependence of the diameter of the central zone for 2 mm drop (46) and jet (equivalent drop size ~4 mm) impact. The ratio is close to the factor 2 which would be predicted.



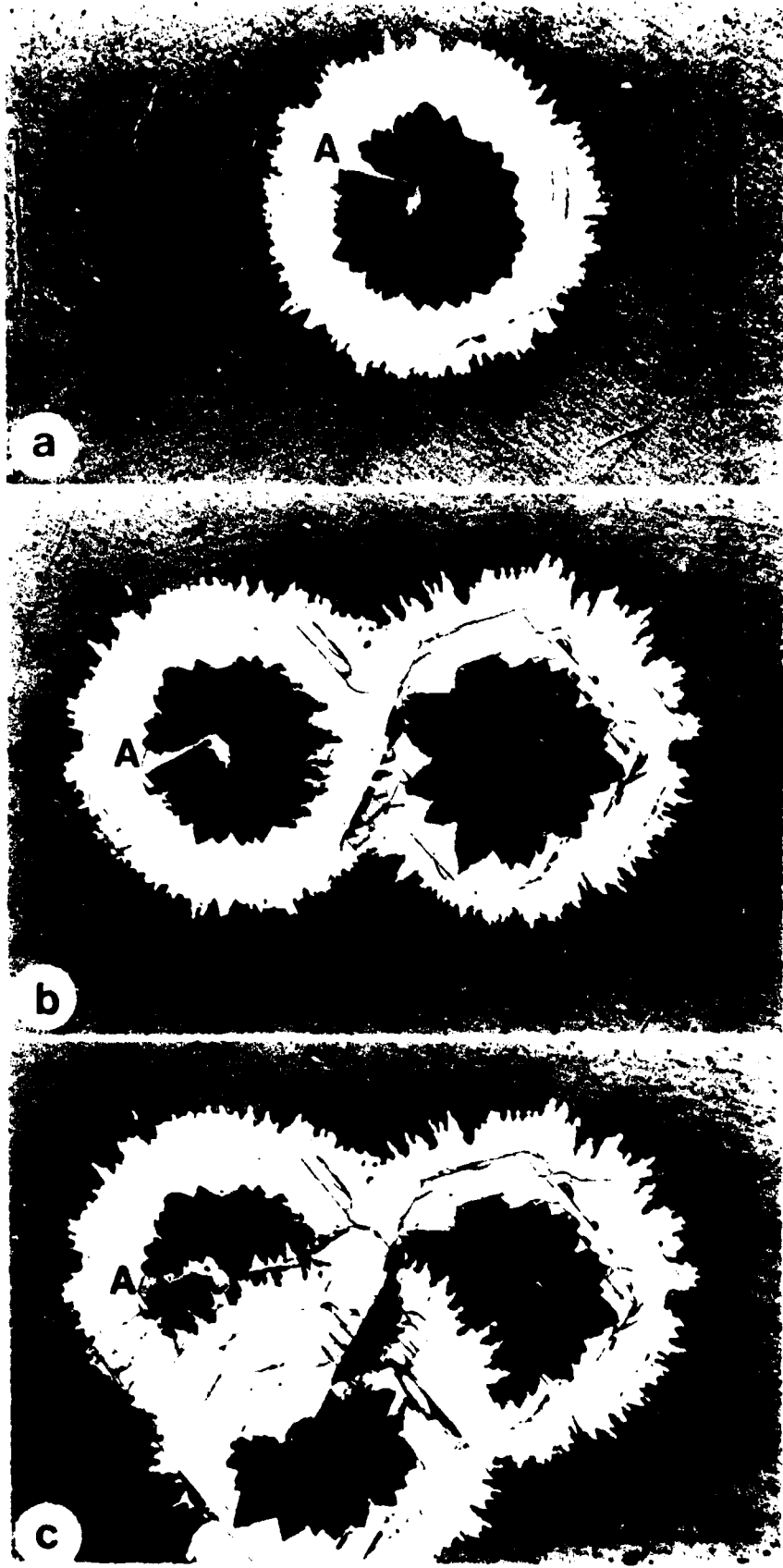
27. Maximum crack depth for 2 mm drop (46) and jet (equivalent drop size ~4 mm) impact. The ratio is close to the factor 2 which would be predicted.



28. Variation of the load to form ring cracks as a function of ball radius for both uncoated and coated germanium.



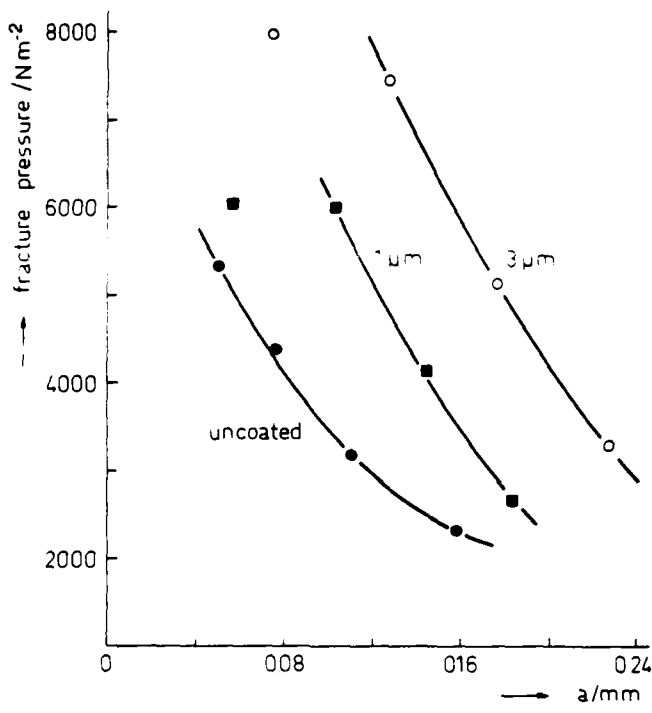
29. Impact damage on uncoated germanium due to a 0.8 mm jet. Impact velocity 260 m s^{-1} . (a) damage after first impact, (b) damage after second impact, (c) damage after third impact. The letter A marks a common feature in each figure to aid in the comparison.



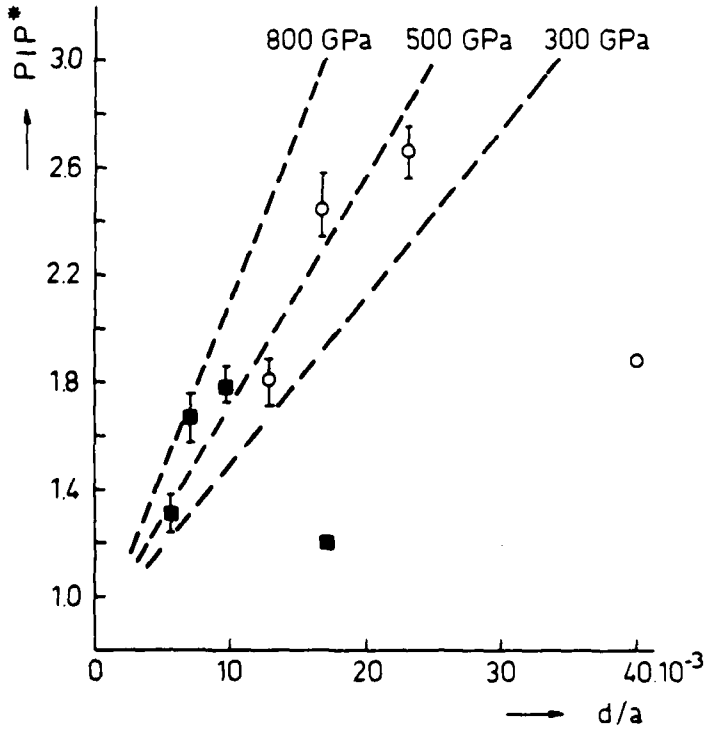
30. Impact damage on 3 μm coated germanium due to a 0.8 mm jet. Impact velocity
 260 m s^{-1} as for Figure 2.



31. Damage due to three consecutive impacts at 220 m s^{-1} on (a) uncoated germanium, (b) $3 \mu\text{m}$ coated germanium.



32. Variation of pressure at which ring crack formed as a function of contact radius for both uncoated and coated germanium (same data as in Figure



33. Ratio of the fracture pressure for coated and uncoated specimens as a function of the normalised coating thickness (see text).

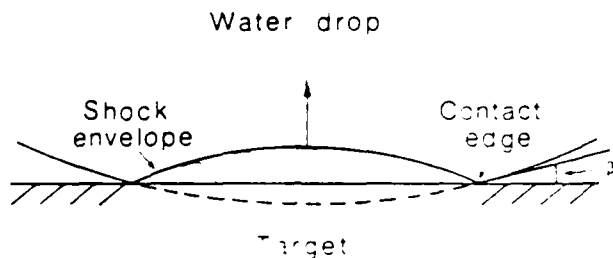
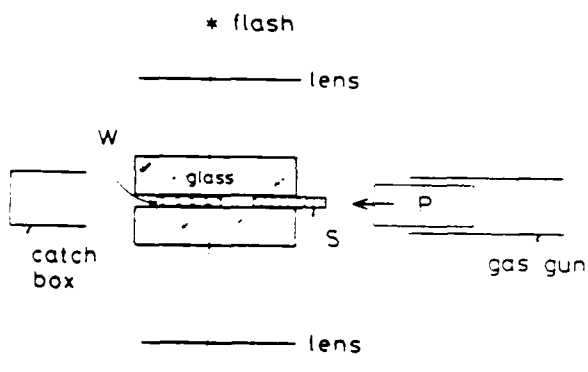
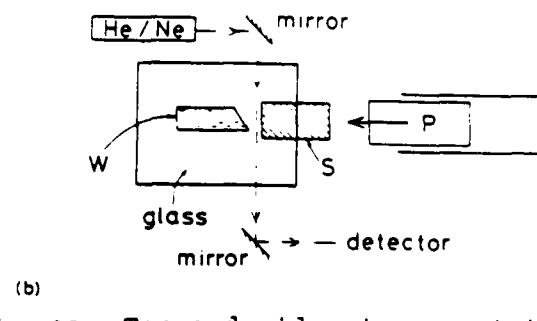


Fig. 34. Impact of a drop with a target. The shock envelope is constructed from many individual wavelets. With a drop the angle β constantly changes.



(a)



(b)

Fig. 35. Top and side views, not to scale, of the impact geometries. W is the liquid/gelatine wedge, P is the plastic sabot and S the impacting striker. In the initial experiments S was stationary and P was fired from a circular bore gun. In the final arrangement S was projected from a two-dimensional gun and higher impact velocities with W were achieved.

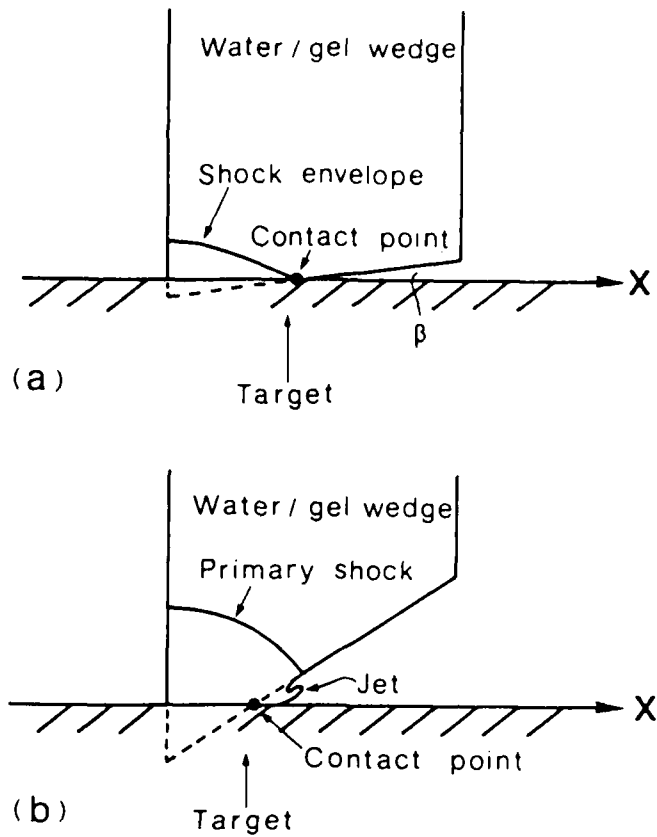


Fig. 36. Impact geometries for a target striking a liquid wedge for (a) supersonic contact with the shock envelope attached to the contact point (b) subsonic contact with the primary shock advancing ahead of the contact point and a jet forming.

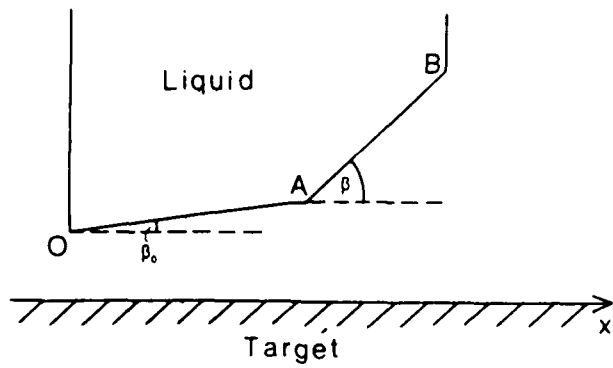
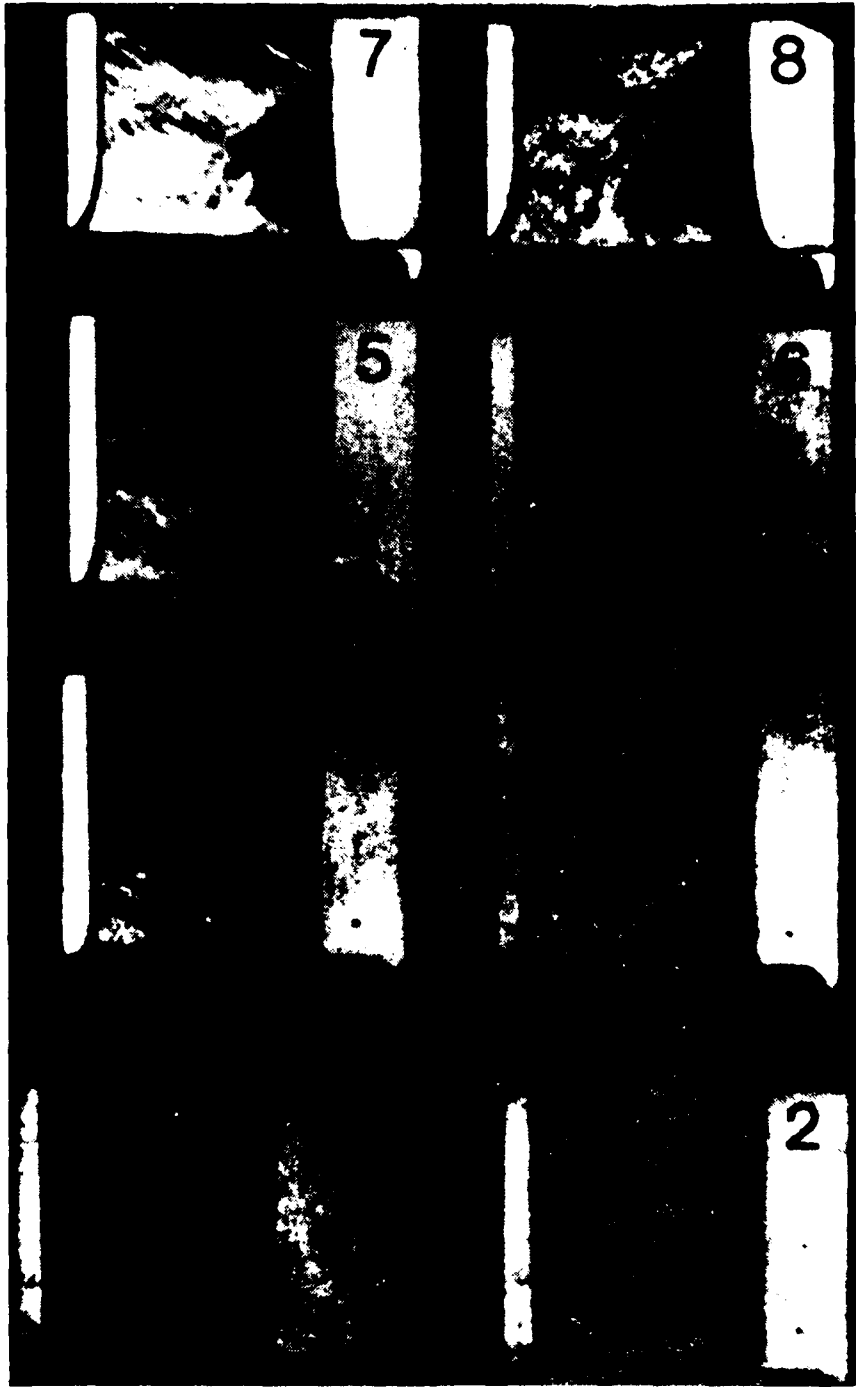
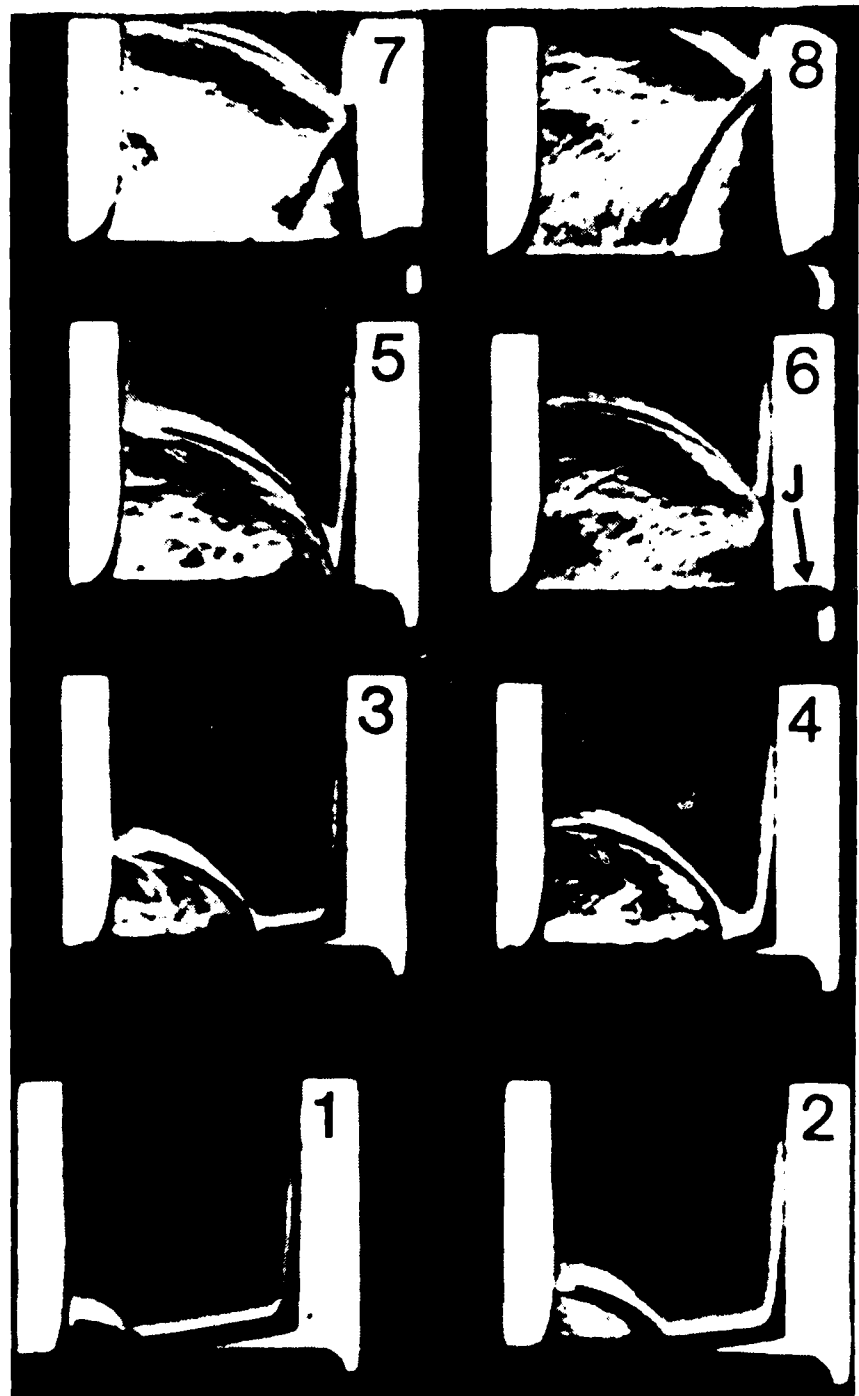


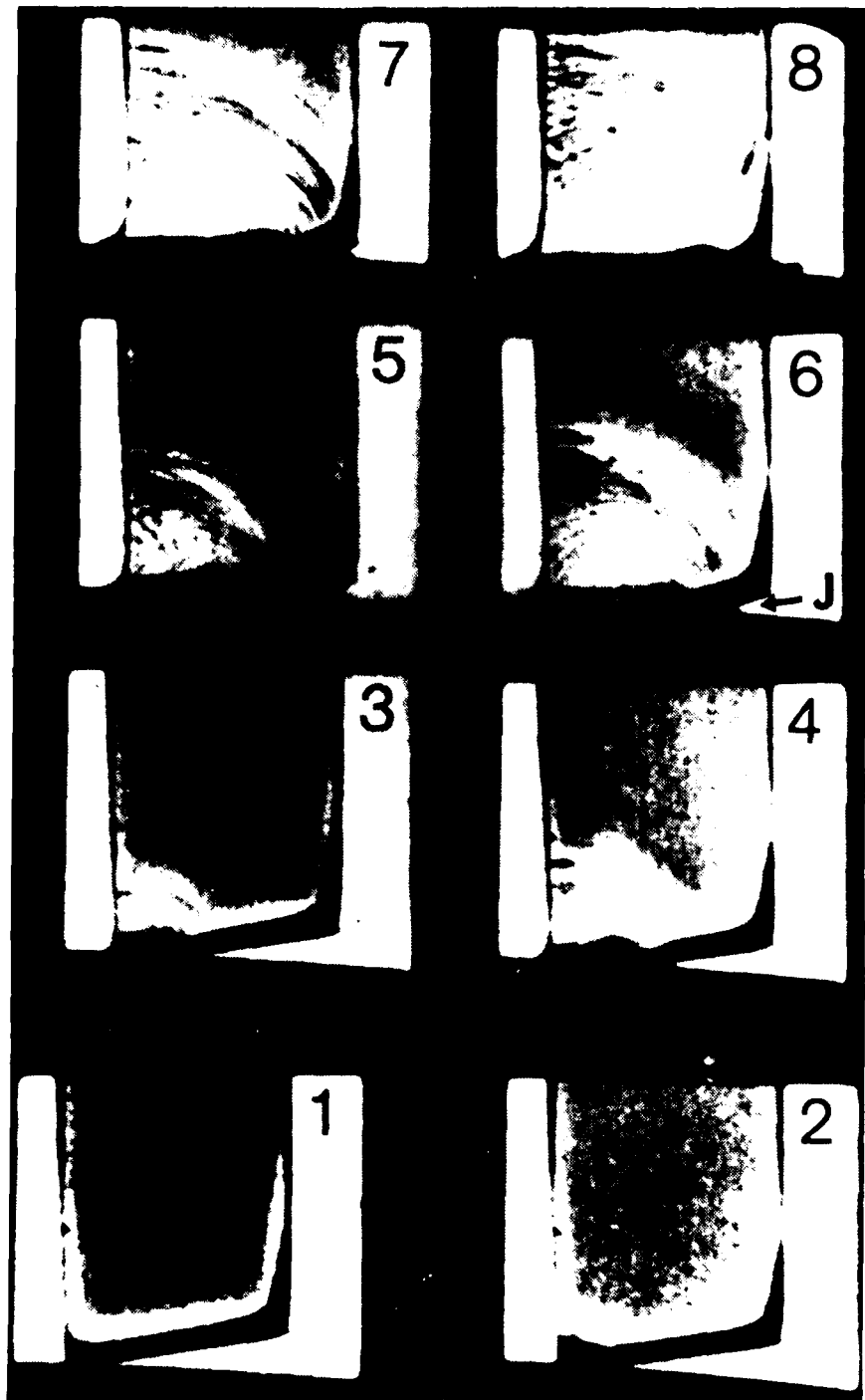
Fig. 41. Impact with a double-angled wedge with $\beta_0 < \beta_c$ and β variable in the range β_c to 90° .



37. Impact with a wedge-shaped specimen. There is a superficial crack (7) jetting in the wedge. This crack occurs only when the wedge is not perfectly sharp. The jet crack is a useful inspection of the wedge-shaped specimen. The damage is due to cavitation.



38. Impact with a wedge - ca. 6° and $M_1 = 10$. This is very close to the critical value for α . A strong shock is formed. Again there is no jetting in the wedge but only when the shock reaches the left-hand boundary. The jet labelled J, has a velocity of ca. 2500 m s^{-1} .

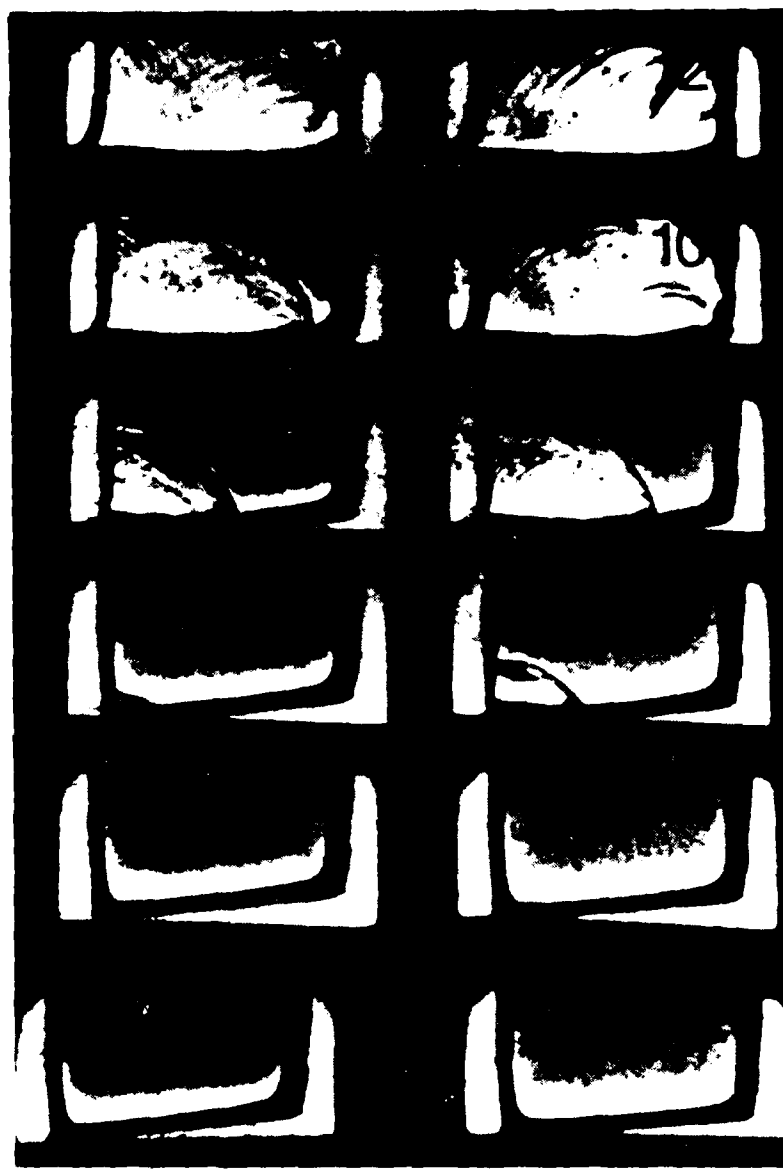


39. *Urolophus* sp.

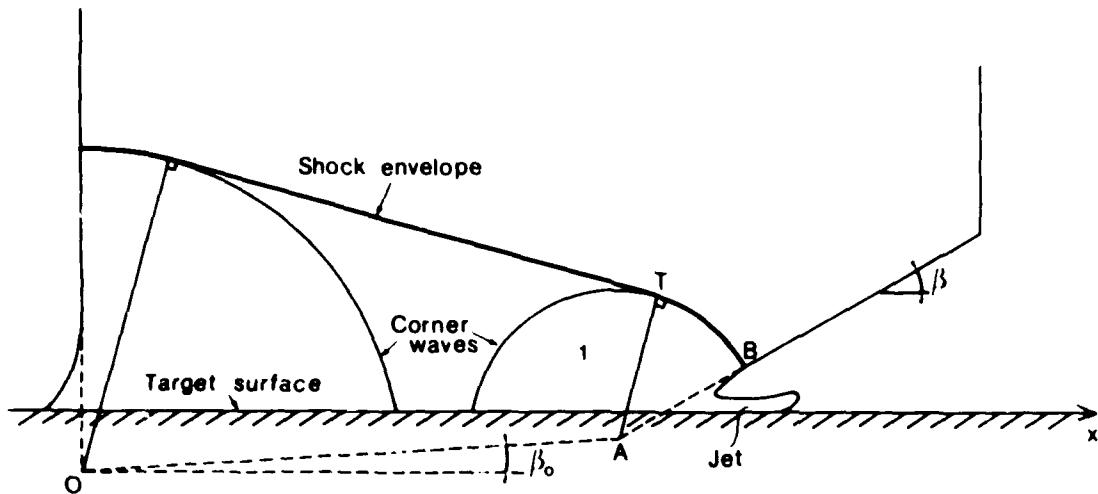
Counts of 1000

Specimens from California

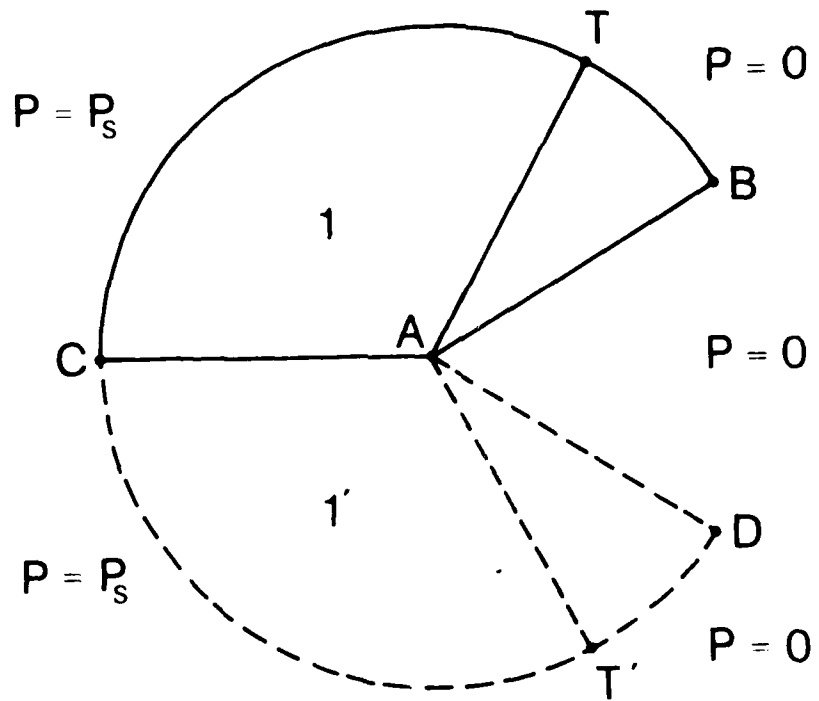
Lengths in millimeters



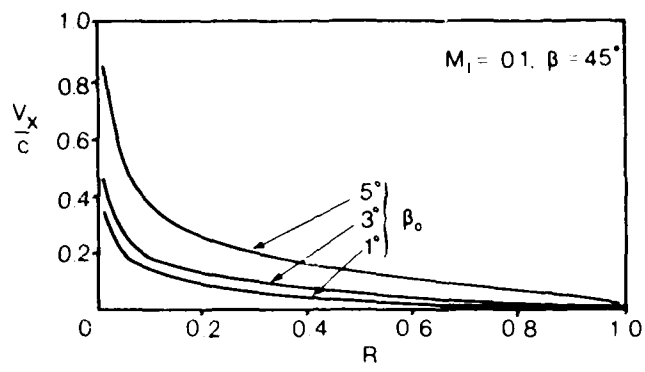
40. Dental casts of upper teeth of a patient with a high arch and M_1 = C.I. 2. Note the presence of a diastema between the upper central and lateral incisors and the absence of the upper canine. The upper molars are slightly rotated at M_1 and M_2 .



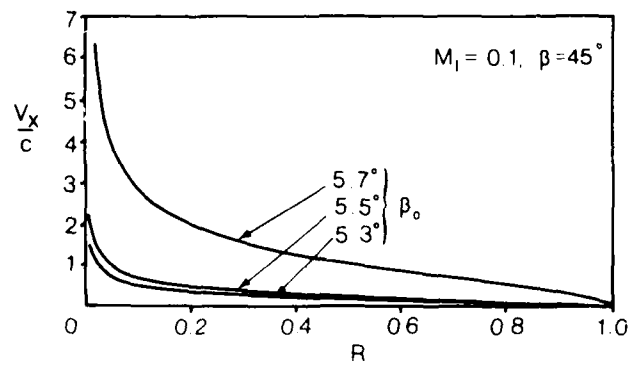
42. Situation when the target surface has passed point A and jetting has commenced. The positions of the shock envelope and the corner waves from O and A are shown.



43. Region 1 from Figure 42 is redrawn together with its image region 1'. The pressures on the various boundaries are indicated.



(a)



(b)

44. The x-component of the flow velocity plotted non-dimensionally in terms of position along the line AB (figure 42), for various double-edge configurations. $R = 0$ corresponds to point A, and $R = 1$ to point B. Note the dramatic increase in V_x as $f_c(5.7)^0$ is approached)

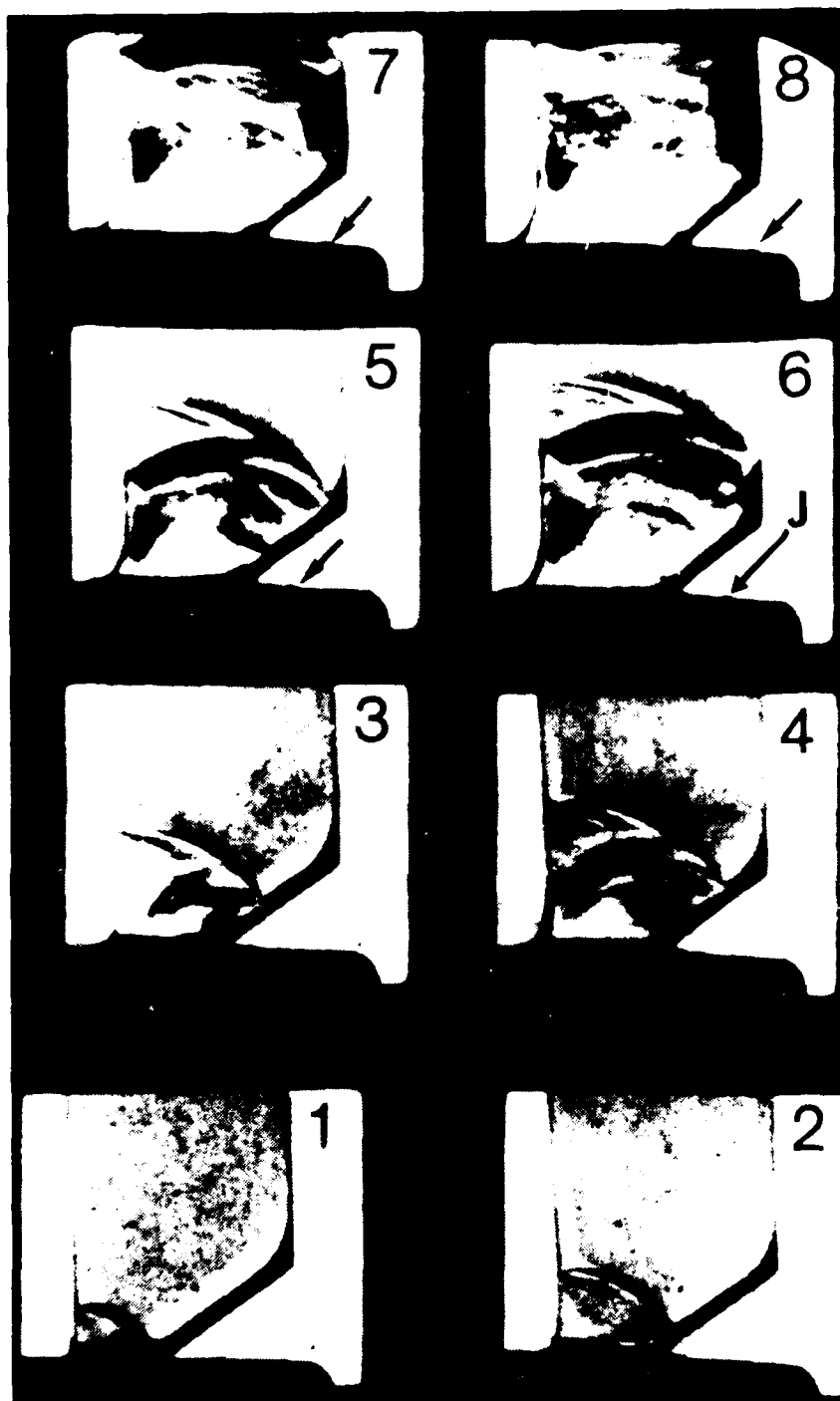


Fig. 1. An example of impact with a double-angle wedge with $\gamma = 1.4$, $\gamma_{\infty} = 1.4$, c_{∞} critical and $\gamma = 45^\circ$. The airway rank the jet which has a velocity of $c = 100 \text{ m s}^{-1}$ in agreement with the inv.

END
DATE
FILMED

1 - 84

DTIC